J. Fluid Mech. (2007), *vol.* 576, *pp.* 139–172.
doi:10.1017/S0022112006003867 Printed in the United Kingdom

Lubrication theory for electro-osmotic flow in a non-uniform electrolyte

T. L. SOUNART† AND J. C. BAYGENTS

Department of Chemical and Environmental Engineering, The University of Arizona, Tucson, AZ 85721, USA

(Received 1 March 2005 and in revised form 7 August 2006)

A lubrication theory has been developed for the electro-osmotic flow of non-uniform buffers in narrow rectilinear channels. The analysis applies to systems in which the transverse dimensions of the channel are large compared with the Debye screening length of the electrolyte. In contrast with related theories of electrokinetic lubrication, here the streamwise variations of the velocity field stem from, and are nonlinearly coupled to, spatiotemporal variations in the electrolyte composition. Spatially non-uniform buffers are commonly employed in electrophoretic separation and transport schemes, including iso-electric focusing (IEF), isotachophoresis (ITP), field-amplified sample stacking (FASS), and high-ionic-strength electro-osmotic pumping. The fluid dynamics of these systems is controlled by a complex nonlinear coupling to the ion transport, driven by an applied electric field. Electrical conductivity gradients, attendent to the buffer non-uniformities, result in a variable electro-osmotic slip velocity and, in electric fields approaching $1\,\mathrm{kV\,cm^{-1}}$, Maxwell stresses drive the electrohydrodynamic circulation. Explicit semi-analytic expressions are derived for the fluid velocity, stream function, and electric field. The resulting approximations are found to be in good agreement with full numerical solutions for a prototype buffer, over a range of conditions typical of microfluidic systems. The approximations greatly simplify the computational analysis, reduce computation times by a factor 4–5, and, for the first time, provide general insight on the dominant fluid physics of two-dimensional electrically driven transport.

1. Introduction

Microfluidic technology involves the manipulation of fluids on submillimetre length scales. One of the most promising applications of microfluidics is the 'lab-on-a-chip' device, which is expected to revolutionize analytical chemistry much as the integrated circuit revolutionized the microelectronics industry (Mitchell 2001; Stone, Stroock & Ajdari 2004). With this rapidly emerging technology, the physical and chemical processes required of a chemical analysis are miniaturized, multiplexed, and integrated onto a microchip. A fundamental challenge in developing microfluidic systems is the precise control of fluid motion through networks of microchannels. Flows in these networks are typically on the order of nanolitres per second, and many microfluidic processes require flow control to picolitres-per-second accuracy (Bousse *et al.* 2000). While microscale mechanical pumps have failed in this to date, a pumping

† Author to whom correspondence should be addressed. Present address: Intel Corporation, 4500 Dobson Rd, Chandler, AZ 85248, USA. thomas.l.sounart@intel.com

mechanism that has been demonstrated to be capable of this is electro-osmosis (Bousse *et al.* 2000), which arises naturally when an electric potential gradient is imposed along a narrow electrolyte-filled channel. Electro-osmotic fluid motion is produced by electrical stresses in the diffuse charge layer near a charged interface; the applied electric field imparts motion to the ions, which transfer momentum to the bulk fluid through molecular interactions. It is thus a natural choice for microfluidic systems, which typically require applied potential gradients for electrophoretic separations.

Theories of electrokinetic motion began with the work of von Helmholtz (1879) and von Smoluchowski (1903), who developed formulae relating the electrophoretic and electro-osmotic velocities to the surface potential and applied electric field in the thin double-layer and low-zeta-potential limit. More general theories have followed (Russel, Saville & Schowalter 1989; Ghosal 2004), but until recently most of the effort has been focused on linear theory. Analytical solutions have elucidated much of the underlying physics and chemistry of electrophoresis and electro-osmosis but have limited utility in predicting the behaviour of inherently nonlinear microfluidic processes.

A general set of nonlinear balance laws for electrophoretic separations was first introduced by Bier *et al.* (1983) in the early 1980s. The Bier group later developed a one-dimensional simulation of the classical modes of electrophoretic separation (Saville & Palusinski 1986; Palusinski *et al.* 1986; Mosher, Saville & Thormann 1992), and since then many researchers have used similar one-dimensional simulations to advance our understanding of the dynamics of electrophoresis (e.g. Kasicka 1997; Gebauer & Bocek 2002). Strictly one-dimensional models make it difficult to account for effects, such as solute dispersion, that are associated with non-uniform electro-osmosis and common to electrically driven separations. Sounart & Baygents (2001) thus extended the Bier *et al.* model to two dimensions and incorporated non-uniform electro-osmosis to examine nonlinearly coupled solute dispersion and fluid motion in microfluidic channels. These unsteady simulations of electrokinetic motion in multiple dimensions are computationally intensive – at electric field strengths of hundreds to thousands of $\mathrm{V\,cm^{-1}}$, sharp gradients in the field variables form locally and fine meshes and/or flux-limiter techniques (Sweby 1984) are required for convergence. Moreover, two elliptic PDEs (one for the fluid velocity $\boldsymbol{u}$ and one for the electric potential ϕ) and a system of nonlinear algebraic equations and parabolic PDEs (for the solutal concentrations) must be solved simultaneously at each point in a three-dimensional (or four-dimentional) spatiotemporal computational domain. The application of flux-corrected transport (FCT) to the electrophoresis model has permitted the simulation of some processes (Sounart & Baygents 2000, 2001), but many more complicated systems remain intractable. Adaptive non-uniform grids may improve computational efficiency enough to conquer these systems, but many challenges to the development of such algorithms for electrophoresis simulations exist.

An alternative approach to computational development is to implement approximations in a problem formulation that simplifies the calculation without excising the essential physics and chemistry. Bharadwaj & Santiago (2005) used cross-sectional averaging to develop one-dimensional macrotransport approximations of coupled electrokinetic and electro-osmotic motion for dilute analytes stacking in a binary electrolyte with an axial conductivity gradient. They applied this model to investigate the dynamics of the stacking boundary in field-amplified sample stacking (FASS). Their parametric studies reveal optimum operating conditions, and the model results are shown to compare qualitatively well with the experimental data.

Here we present a lubrication theory for two-dimensional electro-osmosis and electrohydrodynamics in a microchannel, emphasizing the motion that results from

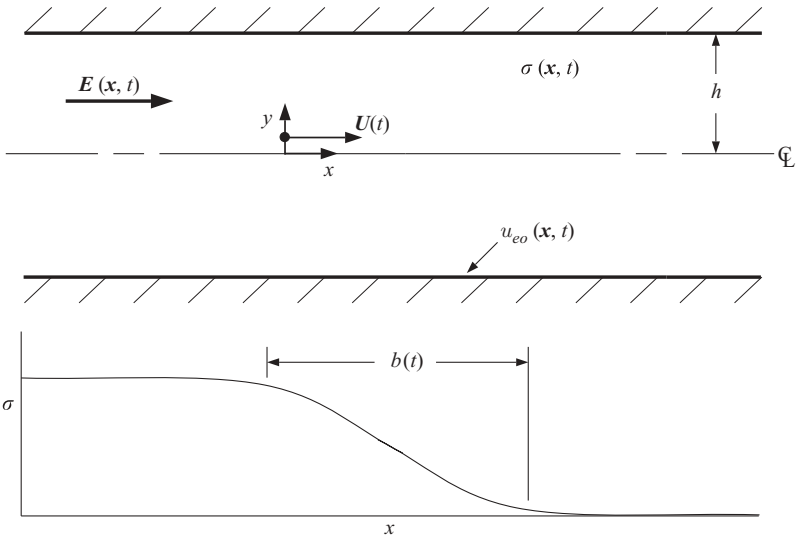

FIGURE 1. Definition sketch for two-dimensional electro-osmotic flow in a non-uniform electrolyte. A rectangular channel of infinite extent perpendicular to the (x, y)-plane is filled with a spatiotemporally variable electrolyte and subjected to an applied electric field in the x-direction. The characteristic length $b(t)$ for axial conductivity variations is time dependent owing to dispersion, and the approximate solutions apply when $(h/b)^2 \ll 1$, $(h/b)^3 Pe \ll 1$, $(h/b)Re \ll 1$. Because of the high aspect ratio, the diagram is not to scale; in particular the width of the channel is exaggerated.

streamwise gradients in the electrical conductivity of the fluid. Consider a long channel formed by parallel surfaces separated by a distance $2h$, as shown in figure 1; the channel is filled with an electrolyte of non-uniform composition and, as a consequence, the electrical conductivity σ varies axially over a characteristic length b. For electro-osmotic flow in a microchannel, the fluid velocity $\boldsymbol{u}$ and electric field $\boldsymbol{E} \equiv -\nabla\phi$ are coupled to σ, so b is also the axial length scale for variations in $\boldsymbol{u}$ and $\boldsymbol{E}$. Solute-dispersion mechanisms dictate that b is, in many cases, large relative to h (Thormann *et al.* 1998; Mosher *et al.* 1992; Burgi & Chien 1991). Also, on microfluidic length scales, $\boldsymbol{u}$ and $\boldsymbol{E}$ are often quasi-steady, viz. the fluid motion and electric field adjust to changing ion distributions on time scales that are small relative to the time scales for ion transport. In such instances, if the Peclet number Pe is not too large, specifically if $(h/b)^3 Pe \ll 1$, the classical lubrication approximation $(h/b)^2 \ll 1$ simplifies the problem formulation, and explicit semi-analytic expressions for $\boldsymbol{u}$ and $\boldsymbol{E}$ are obtained in terms of the ion distributions at any given time. The expressions are semi-analytic because the balance laws governing the ion distributions are nonlinear and must be solved numerically.

A few other researchers have used lubrication theory in the context of electro-osmotic flow. Ajdari (1996) and Long, Stone & Ajdari (1999) considered the lubrication-approximation limit in treatments of electro-osmotic flow between parallel plates with surface undulations and/or charge variations. Ghosal (2002) presented a lubrication theory for electro-osmotic flow in a microchannel of arbitrary shape and slowly varying cross-section and wall charge. This was later coupled with a model for wall adsorption in capillary-zone electrophoresis (Ghosal 2003). The theory presented here differs markedly from those works because the two-dimensional fluid motion stems from non-uniformities in the electrolyte rather than from the surface properties

or channel geometry. Consequently, $\boldsymbol{u}$ and $\boldsymbol{E}$ are coupled to the two-dimensional nonlinear ion transport, and the characteristic scales in the problem are dictated in part by the electrolyte properties. Electrohydrodynamic stresses, two-dimensional conductivity fields, protonation–deprotonation reactions, and diffusion currents acting within the fluid volume must also be considered, and $\boldsymbol{u}$ and $\boldsymbol{E}$ evolve in time.

The approximations for $\boldsymbol{u}$ and $\boldsymbol{E}$ are evaluated by comparison with simulations of a prototype non-uniform-electrolyte configuration (Sounart & Baygents 2001) and are shown to produce accurate representations of the two-dimensional fluid motion, ion transport, and electric field. In some cases, an approximation error is introduced into a narrow region within a conductivity zone boundary during an initial transient. The error is highly localized, diminishes rapidly, and does not significantly affect the solution at later times. For all configurations examined, the average fluid-speed approximation error in the conductivity transition zones is less than 1 % at all times and is less than 0.2 % after two characteristic times for convection across the sample zone.

Although numerical simulation is still required to calculate the unsteady ion distributions, the computational expense devoted to calculating $\boldsymbol{u}$ and $\boldsymbol{E}$, about 80 % of the total simulation time, is essentially eliminated. The approximations may also lay the foundation for additional approximations that might reduce simulation times further, and permit simulation of more complicated electrolyte systems. For example, a similar approximation to that developed here for $\boldsymbol{u}$ and $\boldsymbol{E}$, may be possible for the pH value, the calculation of which consumes most remaining simulation time. This would reduce two-dimensional simulation times by more than an order of magnitude over that required to solve the full problem and would provide details of the fluid motion and ion transport in electrolyte systems that remain intractable.

The approximate theory presented here also has significance beyond improving computational efficiency. The scaling of the balance laws and the explicit expressions obtained for $\boldsymbol{u}$ and $\boldsymbol{E}$ illuminate the dominant physics of electrically driven transport in microchannels, providing general estimates that are difficult to extract from specific numerical solutions with the full model. The analysis indicates that applied electric fields in straight microchannels are essentially unidirectional, even when the transverse component of the conductivity gradient exceeds the axial component. The approximations show that the transverse component E_y of $\boldsymbol{E}$, though orders of magnitude smaller than the axial component E_x, can nevertheless have a significant effect on the fluid motion. With the lubrication approximation, E_x is calculated to leading order as for a one-dimensional field, using cross-sectionally averaged variables, and E_y is approximated as a function of the transverse diffusion current and of an integral of the conductivity field. The analysis also demonstrates that, where electrical stresses are negligible, the local axial component of the fluid velocity is typically parabolic. At sufficiently high values of $\boldsymbol{E}$, however, the components of $\boldsymbol{u}$ are described by terms analogous to a classical lubrication approximation plus additional electrohydrodynamic terms that involve integrals of the electric field. Simulation results demonstrate that bulk electrical stresses alter the structure of the flow in conductivity zone boundaries, producing complicated circulations heretofore unseen.

The presentation in this paper begins with a summary of the balance laws in § 2 and a general two-dimensional simulation method in § 3. From the scale analysis in § 4 approximate solutions for $\boldsymbol{E}$ and $\boldsymbol{u}$ are developed in § 5 and § 6, respectively, and summarized in § 7. In § 8, the approximations are evaluated by comparing the simulation results to those generated by numerical solutions to the full problem. The paper is then concluded in § 9 with remarks on the implications of the results.

2. Problem formulation

A model describing two-dimensional electrically driven fluid motion in a microchannel was presented in a previous work (Sounart & Baygents 2001). The model consists of a coupled set of balance laws and boundary conditions that are appropriate for electrophoretic separations and related microfluidic processes. The problem formulation is sufficiently general to permit investigation of such processes for a broad set of operating conditions. The configuration considered in this work is shown in figure 1. An electric field is applied with the anode in a buffer reservoir to the left of the channel and a cathode in a reservoir to the right. Under the action of the field, the solvent and M solutal components are transported along the axis of the channel, which is of length L_c. Because the concentrations of the solutes, including the ionic species of the buffer, vary with position and time, so too do $\boldsymbol{u}, \boldsymbol{E}$, and σ. The governing equations that account for these coupled variations are summarized in the subsections that follow; more complete expositions of the balance laws can be found elsewhere, e.g. in Saville & Palusinski (1986), Mosher *et al.* (1992), and Sounart & Baygents (2001).

Before stating the balance laws, we note that we apply these equations to the bulk electrolyte, meaning the fluid that is not within the electrical double layers at the channel walls. To account for electrokinetic motion within the electrical double layers, we apply an electro-osmotic slip condition on u at $y = \pm h$, as indicated in § 2.2.

2.1. *Balance laws*

The motion of the aqueous electrolyte is governed by the Stokes equations, augmented to accommodate electrical stresses, i.e.

$$0 = -\nabla p + \eta \nabla^2 \boldsymbol{u} + \epsilon_0 \epsilon \nabla\phi \nabla^2 \phi, \tag{2.1}$$

$$\nabla \cdot \boldsymbol{u} = 0. \tag{2.2}$$

Here η and ϵ are the fluid viscosity and relative permittivity, respectively, p is the pressure, and ϵ_0 is the permittivity of free space. Typical buffer ionic strengths are 1–100 mM and the Debye screening length κ^{-1} is 1–10 nm. So long as h and b are at least of the order of microns, the bulk charge density ρ_e is zero to leading order at the length scales of interest. The governing equation for the bulk electric potential ϕ then follows from considerations of charge conservation (Mosher *et al.* 1992), viz.

$$\nabla \cdot (\sigma \nabla\phi - \boldsymbol{i}_D) = 0, \tag{2.3}$$

where $-\sigma\nabla\phi$ and $\boldsymbol{i}_D$ represent the ohmic and diffusive contributions to the electrical current, respectively. Despite the fact that $\rho_e \sim 0$, spatial variations of ϕ dictated by (2.3) can give rise to Maxwell stresses that alter the bulk fluid motion, and this is accounted for by the last term on the right-hand side of (2.1).

In an ionic conductor, σ can be described in terms of ionic species concentrations, which evolve due to mass transport and protonation–deprotonation reactions. Because the reactions are fast relative to mass transport, ion concentrations are constrained locally by the mass-action equilibrium relations

$$K_k^z \equiv \frac{[\mathrm{H}^+] n_k^{z-1}}{n_k^z}, \qquad \begin{cases} z = -N_k + 1, -N_k + 2, \ldots, P_k \\ k = 1, 2, \ldots, M, \end{cases} \tag{2.4}$$

where K_k^z and n_k^z are, respectively, the acidic equilibrium constant and the concentration of the subspecies of the kth solutal component with valence z; P_k and N_k are, respectively, the number of cationic and anionic subspecies of the kth component.

The electroneutrality approximation can then be written as

$$\sum_{k=1}^{M} \sum_{z=-N_k}^{P_k} z_k n_k^z + [\mathrm{H}^+] - \frac{K_w}{[\mathrm{H}^+]} = 0, \tag{2.5}$$

where $K_w \equiv [\mathrm{H}^+][\mathrm{OH}^-]$ is the dissociation constant for water.

The effect of fluid motion on the ion concentrations is governed by balance laws for each ionic species. If the transport mechanisms include convection, electromigration, and diffusion, we have

$$\frac{\partial n_k^z}{\partial t} = \nabla \cdot \left[ez\omega_k n_k^z \nabla\phi - n_k^z \boldsymbol{u} + \omega_k k_B T \nabla n_k^z \right] + R_k^z, \qquad \begin{cases} z = -N_k, -N_k + 2, \ldots, P_k, \\ k = 1, 2, \ldots, M. \end{cases} \tag{2.6}$$

In (2.6) t denotes time, $k_B T$ is the Boltzmann temperature, e is the charge on a proton (1.6×10^{-19} C), ω_k is the hydrodynamic mobility, which is approximated as constant for all species of component k, and R_k^z is the rate of generation of n_k^z through mass action. Conservation laws for the solutal components are derived by summing (2.6) over the species index z for each component k, which yields

$$\frac{\partial C_k}{\partial t} = -\nabla \cdot \boldsymbol{f}_k = \nabla \cdot [e\bar{z}_k \omega_k C_k \nabla\phi - C_k \boldsymbol{u} + \omega_k k_B T \nabla C_k], \qquad k = 1, 2, \ldots, M, \tag{2.7}$$

where $\boldsymbol{f}_k$, C_k, and $\bar{z}_k$ are the flux, concentration, and effective valence of component k; $\boldsymbol{f}_k$ is defined implicitly in (2.7), and C_k and $\bar{z}_k$ are defined, respectively, as

$$C_k \equiv \sum_{z=-N_k}^{P_k} n_k^z, \qquad k = 1, 2, \ldots, M, \tag{2.8}$$

and

$$\bar{z}_k \equiv \frac{\displaystyle\sum_{z=-N_k}^{P_k} z n_k^z}{C_k}, \qquad k = 1, 2, \ldots, M. \tag{2.9}$$

The governing equations are closed by relating σ and $\boldsymbol{i}_D$ to the ion concentrations. By combining (2.5) and (2.6) with solvent ion balances, and comparing with (2.3), it can be shown that (Mosher *et al.* 1992)

$$\boldsymbol{i}_D = -ek_B T \left(\sum_{k=1}^{M} \omega_k \nabla \bar{z}_k C_k + \omega_{\mathrm{H}} \nabla [\mathrm{H}^+] - \omega_{\mathrm{OH}} K_w \nabla [\mathrm{H}^+]^{-1} \right) \tag{2.10}$$

and

$$\sigma = e^2 \left[\sum_{k=1}^{M} \overline{z_k^2} \omega_k C_k + \omega_{\mathrm{H}} [\mathrm{H}^+] + \omega_{\mathrm{OH}} \frac{K_w}{[\mathrm{H}^+]} \right], \tag{2.11}$$

where $\overline{z_k^2}$ is the mean-square valence of the kth component, i.e.

$$\overline{z_k^2} \equiv \frac{\displaystyle\sum_{z=-N_k}^{+P_k} z^2 n_k^z}{C_k}, \qquad k = 1, 2, \ldots, M. \tag{2.12}$$

2.2. *Initial and boundary conditions*

We are concerned with microchannel flow driven by the external application of an electric field, as is typical for electrokinetically operated microfluidic systems. Buffer reservoirs at the channel ends $x = x_0$ and $x_0 + L_c$ are thus maintained at the same pressure, so $p(x_0, y, t) = p(x_0 + L_c, y, t)$ is set to an arbitrary constant (zero). Because microfluidic channel depths are typically $O(10\,\mu\text{m})$ and κ^{-1} is typically less than 10 nm, $\kappa h \gg 1$. Electrokinetic motion in the diffuse charge layer near the channel walls is then manifested as an apparent slip condition on the motion of the bulk electrolyte. Since a zone of non-uniform electrolyte is advected down the channel, we adopt a moving frame of reference that translates at a speed $U(t)$. Let $u(x, y, t) \equiv \boldsymbol{u} \cdot \boldsymbol{e}_x$ and $v(x, y, t) \equiv \boldsymbol{u} \cdot \boldsymbol{e}_y$, where $\boldsymbol{e}_x$ and $\boldsymbol{e}_y$ are the unit vectors in the axial and transverse directions, respectively (figure 1). We require

$$u(x, \pm h, t) \equiv u_{eo}(x, t) = \mu(x, t) E_x(x, h, t) - U(t), \qquad v(x, \pm h, t) = 0, \tag{2.13}$$

where the local electro-osmotic mobility for the channel wall, μ, is calculated as a function of ionic strength, pH, and buffer-cation concentration (Thormann *et al.* 1998); the reference-frame speed $U(t)$ is calculated as (Anderson & Idol 1985)

$$U(t) = \frac{1}{L_c} \int_{x_0}^{x_0 + L_c} \mu(x, t) E_x(x, h, t)\, \mathrm{d}x. \tag{2.14}$$

With this formulation, $U(t)$ is the mean velocity of the channel flow for cases where the effect of the bulk Maxwell stresses is negligible.

The entrance length is $O(h) \ll L_c$ for a Stokes flow, so if the uniform buffer at the column ends is undisturbed by variations in the channel interior, there is unidirectional flow at $x = x_0$ and $x_0 + L_c$, viz.

$$u(x_0, y, t) = u(x_0 + L_c, y, t) = \tfrac{3}{2}[u_0 - U(t)]\left[\left(\frac{y}{h}\right)^2 - 1\right] + [u_0 - U(t)] \tag{2.15}$$

and

$$v(x_0, y, t) = v(x_0 + L_c, y, t) = 0. \tag{2.16}$$

In (2.15), $u_0 = \mu_0 E_0$, where u_0 is the electro-osmotic velocity, μ_0 is the electro-osmotic mobility, and E_0 is the magnitude of the electric field, all in the running buffer; u_0 is constant if the electric current in the channel is constant.

The boundary conditions on the electric potential are

$$\left.\begin{aligned} \sigma \nabla\phi \cdot \boldsymbol{n} &= \boldsymbol{i}_D \cdot \boldsymbol{n}, && y = \pm h, \\ \phi &= 0, && x = x_0 + L_c, \\ \sigma \nabla\phi \cdot \boldsymbol{n} &= i_0, && x = x_0 \quad \text{(constant current)}, \\ \phi &= \phi_0, && x = x_0 \quad \text{(constant voltage)}, \end{aligned}\right\} \tag{2.17}$$

where ϕ_0 and i_0 are, respectively, the (constant) potential or axial current density prescribed at the electrodes and $\boldsymbol{n}$ is the unit normal directed outward from the electrodes and the electrically insulating channel walls. The concentrations $C_k, k = 1, 2, \ldots, M$, are fixed at their running buffer values for $x = x_0, x_0 + L_c$. Adjustments in the surface charge density on the channel wall are considered to contribute negligibly to the species balances, therefore

$$\boldsymbol{f}_k(x, \pm h, t) \cdot \boldsymbol{n} = 0, \qquad k = 1, 2, \ldots, M. \tag{2.18}$$

3. General two-dimensional simulation method

A general procedure has been presented previously for numerically solving in two dimensions the mathematical model described above (Sounart & Baygents 2001). Here we summarize and comment on a slight modification to that approach, which will be used in § 8 for comparison with the approximate solutions.

In most electrophoretic separations and many other microfluidic processes, a sample zone of non-uniform electrolyte having characteristic length $L_s \ll L_c$ is carried by the electro-osmotic flow through a channel filled with a uniform buffer. Thus, to save computation time, the simulation domain is restricted to a small region, of $O(L_s)$, that encompasses the non-uniform buffer. This is done simply for computational efficiency and is not a restriction on the model, since the domain size can be increased as necessary to encompass any number or size of non-uniform conductivity zones. New boundaries $x = \pm L_d$ are accordingly set back a distance of $O(10h)$ from the sample zone, where the running buffer remains uniform. The boundary conditions for $\boldsymbol{u}$, ϕ, and C_k, $k = 1, 2, \ldots, M$, at $x = x_0$ and $x_0 + L_c$ are applicable at $x = \pm L_d$ except in the case of constant voltage, where

$$\phi(-L_d, y) = \phi_0 \left(1 + \frac{2L_d - L_c}{\sigma_0 \displaystyle\int_{x_0}^{x_0+L_c} \mathrm{d}x / \langle \sigma \rangle} \right) \quad \text{(constant voltage)}. \tag{3.1}$$

Here $\langle \sigma \rangle$ is the cross-sectionally averaged conductivity.

The quasi-steady velocity field is calculated in the moving coordinate at any given time by introducing the stream function and solving the biharmonic equation with a forcing function resulting from the electrical stresses, viz.

$$\nabla^4 \psi = -\frac{\epsilon_0 \epsilon}{\eta} \left[\frac{\partial \phi}{\partial x} \frac{\partial (\nabla^2 \phi)}{\partial y} - \frac{\partial \phi}{\partial y} \frac{\partial (\nabla^2 \phi)}{\partial x} \right], \tag{3.2}$$

where

$$u = \frac{\partial \psi}{\partial y}, \qquad v = -\frac{\partial \psi}{\partial x}. \tag{3.3}$$

The boundary conditions on ψ are

$$\psi(x, \pm h, t) = 0, \tag{3.4}$$

$$\frac{\partial \psi}{\partial y}(x, \pm h, t) = u_{eo}(x, t) - U(t), \tag{3.5}$$

$$\psi(\pm L_d, y, t) = \tfrac{3}{2} h [u_0 - U(t)] \left[\tfrac{1}{3} \left(\frac{y}{h} \right)^3 - \left(\frac{y}{h} \right) \right] + [u_0 - U(t)] y, \tag{3.6}$$

$$\frac{\partial \psi}{\partial x}(\pm L_d, y, t) = 0. \tag{3.7}$$

Appropriate numerical methods have been chosen to solve each balance law. An FCT algorithm (Sounart & Baygents 2000) with operator splitting (Gottlieb 1972; Boris *et al.* 1993) was used to solve the parabolic PDEs (2.7), and publicly available subroutines (de Zeeuw 1990; Bjorstad 1983) were incorporated into the main code to solve the elliptic PDEs (2.3) and (3.2). For simulations with buffer B (see § 8), the numerical scheme used to solve the component mass balances (2.7) was slightly modified to increase the computational efficiency. Since diffusion dominates ion

transport in the transverse direction, the transverse finite-difference equation resulting from the operator split is solved implicitly; the time derivative is discretized with a first-order backward-difference approximation, and FCT is not implemented. Since all numerical results presented in this paper are converged, this does not affect any of the comparisons.

4. Scale analysis

An axial conductivity transition, or zone boundary, in a microchannel or capillary is a basic element of most electrophoretic separation processes, e.g. ITP, IEF, and sample stacking (Mosher *et al.* 1992; Beckers & Boček 2000), as well as other microfluidic processes such as high-ionic-strength electro-osmotic pumping (Bousse *et al.* 2000). In these protocols, multiple zones of different composition and conductivity are established along the separation axis. In this section, the system of PDEs that describes the electrically driven transport processes, (2.1)–(2.3) and (2.7), is scaled for an arbitrary zone boundary of length b in a rectangular channel of arbitrary electrolyte composition. The complexity of the following scale analysis results from the many coupled dependent variables that evolve temporally in two dimensions. Scaling arguments are presented first for the variables in the charge balance (2.3). This produces characteristic scales for $E_x \equiv \boldsymbol{E}\cdot\boldsymbol{e}_x \equiv -\partial\phi/\partial x$ and $E_y \equiv \boldsymbol{E}\cdot\boldsymbol{e}_y \equiv -\partial\phi/\partial y$, which are required to scale the electrical stresses in the momentum balance (2.1). After scaling the Stokes equations (2.1) and (2.2), the characteristic values thus derived are applied to scale the component mass balances (2.7). With the scaled balance laws from this section we will derive in the following section the approximate solutions that are possible for geometries and electrolyte configurations typical of electrophoretic separations and related microfluidic processes.

4.1. *Charge balance*

The construction of approximate solutions for $\boldsymbol{u}(\boldsymbol{x}, t)$ and $\boldsymbol{E}(\boldsymbol{x}, t)$ begins with (2.3), which is written as

$$\frac{\partial}{\partial x}(\sigma E_x) + \frac{\partial}{\partial y}(\sigma E_y) = -\frac{\partial i_D}{\partial x} - \frac{\partial j_D}{\partial y}, \tag{4.1}$$

where $i_D \equiv \boldsymbol{i}_D\cdot\boldsymbol{e}_x$ and $j_D \equiv \boldsymbol{i}_D\cdot\boldsymbol{e}_y$. Characteristic scales for some variables in this equation are not obvious from the geometry and initial conditions but can be deduced through physical arguments and simplified expressions.

Diffusion current and conductivity

Characteristic scales for the components of the diffusion current follow from their definition in (2.10). For components of $O(1)$ valence,

$$i_D \sim e k_B T \Delta\omega_c \frac{\delta C_b}{\delta x}, \tag{4.2}$$

where C_b is the buffer concentration and $\Delta\omega_c$ is a characteristic mobility difference of the buffer ions. $\Delta\omega_c$ is $O(\omega_c)$, where ω_c is a characteristic mobility, unless all buffer ions have mobilities that differ by less than $O(\omega_c)$; we will keep track of it as $\Delta\omega_c$ to allow for this special case. By inspection of (2.11), we can relate C_b to σ by $\sigma \sim e^2\omega_c C_b$, which yields

$$i_D \sim \frac{\Delta\omega_c}{\omega_c}\frac{k_B T}{e}\left|\frac{1}{\gamma_2} - \frac{1}{\gamma_1}\right|\frac{\sigma_0}{b} \tag{4.3}$$

for a zone boundary of length b that separates a region of conductivity σ_0/γ_1 from one of conductivity σ_0/γ_2.

Similarly,

$$j_D \sim \frac{\Delta\omega_c}{\omega_c}\frac{k_B T}{e}\frac{\delta\sigma}{\delta y}. \tag{4.4}$$

The proper scaling for $\delta\sigma/\delta y$ follows from the observation that concentration and conductivity variations in the transverse direction, even if initially zero, develop from the fluid motion (Sounart & Baygents 2001). To characterize this, let $\hat{\sigma} \equiv \sigma - \langle\sigma\rangle$ and $\hat{C}_k \equiv C_k - \langle C_k\rangle$, where the angle brackets denote a cross-sectional average. The perturbations $\hat{\sigma}$ and $\hat{C}_k$ are produced by axial convection and limited by transverse diffusion; for $t \gg h^2/(\omega_k k_B T)$, Taylor's approximation (1953) gives

$$\omega_k k_B T \frac{\partial^2 \hat{C}_k}{\partial y^2} \sim u\frac{\partial C_k}{\partial x}, \qquad k = 1, 2, \ldots, M. \tag{4.5}$$

Since the appropriate axial and transverse length scales are b and h, respectively, and the scales for u and C_k are $u_0\,|\,\gamma_2 - \gamma_1\,|$ and $C_0|1/\gamma_2 - 1/\gamma_1|$, respectively, to balance terms in (4.5) we require

$$\hat{C}_k \sim \left(\frac{h}{b}\right) Pe_k \left|\frac{1}{\gamma_2} - \frac{1}{\gamma_1}\right| C_0, \qquad k = 1, 2, \ldots, M, \tag{4.6}$$

where

$$Pe_k \equiv \frac{|\gamma_2 - \gamma_1| u_0 h}{\omega_k k_B T}, \qquad k = 1, 2, \ldots, M. \tag{4.7}$$

Moreover

$$\hat{\sigma} \sim \left(\frac{h}{b}\right) Pe \left|\frac{1}{\gamma_2} - \frac{1}{\gamma_1}\right| \sigma_0, \tag{4.8}$$

where $Pe = Pe_k$ for a characteristic buffer component. According to (4.4), the characteristic value for j_D is therefore

$$j_D \sim \left(\frac{\Delta\omega_c}{\omega_c}\right)\frac{k_B T}{e}\left|\frac{1}{\gamma_2} - \frac{1}{\gamma_1}\right|\frac{\sigma_0}{b} Pe \sim Pei_D. \tag{4.9}$$

Note that the characteristic scales for σ and $\hat{\sigma}$ are not, in general, equivalent; rather,

$$\frac{\hat{\sigma}}{\sigma} \sim \left(\frac{h}{b}\right) Pe. \tag{4.10}$$

Transverse-conductivity variations scale on the Peclet number, which couples the scaling of the charge balance to the fluid motion and ion transport.

Electric field

We now have characteristic values for all variables in (4.1) except E_x and E_y. The characteristic value for E_x is simply

$$E_x \sim |\gamma_2 - \gamma_1| E_0. \tag{4.11}$$

Because the electric field is applied axially, E_y is initially zero if the initial ion concentration fields are cross-sectionally uniform. Non-zero values of E_y are induced by the developing transverse conductivity gradients and the attendant transverse diffusion

current. Thus $\sigma E_y \sim j_D$, or

$$E_y \sim \left(\frac{\Delta\omega_c}{\omega_c}\right)\frac{k_BT}{e}\frac{Pe}{b}. \tag{4.12}$$

If the foregoing scale factors are introduced into (4.1), one obtains

$$\frac{\partial}{\partial x^*}\left[\langle\sigma^*\rangle E_x^* + \left(\frac{h}{b}\right)Pe\hat{\sigma}^* E_x^*\right] + \Gamma\left[\langle\sigma^*\rangle\frac{\partial E_y^*}{\partial y^*} + \left(\frac{h}{b}\right)Pe\frac{\partial}{\partial y^*}(\hat{\sigma}^* E_y^*)\right] = -\Lambda\frac{\partial i_D^*}{\partial x^*} - \Gamma\frac{\partial j_D^*}{\partial y^*}, \tag{4.13}$$

where

$$x^* \equiv \frac{x}{b}, \quad y^* \equiv \frac{y}{h},$$
$$\langle\sigma^*\rangle \equiv \frac{\langle\sigma\rangle}{|1/\gamma_2 - 1/\gamma_1|\sigma_0}, \quad \hat{\sigma}^* \equiv \frac{\hat{\sigma}}{(h/b)Pe|1/\gamma_2 - 1/\gamma_1|\sigma_0},$$
$$E_x^* \equiv \frac{E_x}{|\gamma_2 - \gamma_1|E_0}, \quad E_y^* \equiv \frac{E_y b}{(\Delta\omega_c/\omega_c)(k_BT/e)\,Pe},$$
$$i_D^* \equiv \frac{i_D b}{(\Delta\omega_c/\omega_c)(k_BT/e)\,|1/\gamma_2 - 1/\gamma_1|\sigma_0},$$
$$j_D^* \equiv \frac{j_D b}{(\Delta\omega_c/\omega_c)(k_BT/e)\,|1/\gamma_2 - 1/\gamma_1|\sigma_0 Pe}.$$

In (4.13),

$$\Gamma \equiv \left(\frac{\Delta\omega_c}{\omega_c}\right)\left(\frac{\mu_0}{\omega_c e}\right) \qquad \text{and} \qquad \Lambda \equiv \left(\frac{\Delta\omega_c}{\omega_c}\right)\left(\frac{k_BT/e}{|\gamma_2 - \gamma_1|E_0 b}\right)$$

are dimensionless groups that essentially characterize, respectively, the ratio of the electro-osmotic and electrophoretic mobilities in the running buffer and the ratio of the Boltzmann potential and the characteristic potential drop over the length scale b. The factor $\Delta\omega_c/\omega_c$ is typically $O(1)$ and is included here because we will also consider the special case $\Delta\omega_c \ll \omega_c$. The ratio $\mu_0/(\omega_c e)$ is also typically $O(1)$ unless electro-osmosis is suppressed, in which case $\mu_0/(\omega_c e) < O(1)$. Hence $\Gamma \leqslant O(1)$. Applied-voltage gradients in excess of 100 V cm^{-1} are common in microfluidic systems, so $E_0 b$ is such that $\Lambda \ll 1$.

Transverse perturbation of E_x

The quasi-static electric field is irrotational, or equivalently

$$\frac{\partial E_x}{\partial y} = \frac{\partial E_y}{\partial x}. \tag{4.14}$$

E_x is scaled with $|\gamma_2 - \gamma_1|E_0$, which characterizes the change in E_x over the axial length scale b. But the transverse variations in E_x are small relative to $|\gamma_2 - \gamma_1|E_0$, thus $\partial E_x^*/\partial y^*$ is not $O(1)$. As was done for the conductivity and component concentrations in § 4.1, a new dependent variable $\hat{E}_x \equiv E_x - \langle E_x\rangle$ is introduced; $\hat{E}_x$ changes by $O(\hat{E}_x)$ over the transverse length scale h. With this substitution, (4.14) is scaled and balanced, i.e.

$$\frac{\partial \hat{E}_x^*}{\partial y^*} = \frac{\partial E_y^*}{\partial x^*} \tag{4.15}$$

where $\hat{E}_x^* \equiv \hat{E}_x/(h/b)^2\,\Gamma|\gamma_2-\gamma_1|E_0$. Accordingly,

$$E_x^* = \langle E_x^* \rangle + \left(\frac{h}{b}\right)^2 \Gamma \hat{E}_x^*. \tag{4.16}$$

Since typically $\Gamma \leqslant O(1)$, (4.16) implies that $E_x^* \approx \langle E_x^* \rangle$ for $(h/b)^2 \ll 1$, which is the same stipulation on the lubrication approximation as that for $\boldsymbol{u}(\boldsymbol{x}, t)$ in the Stokes equations. Moreover, comparing (4.16) with (4.10) gives the general result that for $Pe \geqslant O(1)$ the transverse perturbation of the electric field is smaller than that of the conductivity if $h/b < 1$; specifically,

$$\frac{\hat{E}_x/E_x}{\hat{\sigma}/\sigma} \sim \left(\frac{h}{b}\right)\frac{\Gamma}{Pe}. \tag{4.17}$$

Examples of this were obtained previously in numerical simulations (Sounart & Baygents 2001). $\hat{E}_x/E_x$ is independent of Pe, because this is an electrically driven flow, and thus both $\hat{E}_x$ and E_x scale with Pe.

4.2. *Stokes equations*

Scaling arguments from the preceding section also help to scale the Stokes equations. Equation (2.2) reads

$$\frac{\partial u^*}{\partial x^*} + \frac{\partial v^*}{\partial y^*} = 0, \tag{4.18}$$

where $u^* \equiv u/(|\gamma_2-\gamma_1|u_0)$ and $v^* \equiv vb/(|\gamma_2-\gamma_1|u_0 h)$. The scale for v is chosen to satisfy continuity for a two-dimensional flow. Similarly, the momentum balance ((2.1)) becomes

$$\left(\frac{h}{b}\right)^2 \frac{\partial^2 u^*}{\partial x^{*2}} + \frac{\partial^2 u^*}{\partial y^{*2}} + \left(\frac{h}{b}\right)\lambda E_x^*\left[\frac{\partial E_x^*}{\partial x^*} + \Gamma\frac{\partial E_y^*}{\partial y^*}\right] = \frac{\partial p^*}{\partial x^*} \tag{4.19}$$

and

$$\left(\frac{h}{b}\right)^2\left[\left(\frac{h}{b}\right)^2 \frac{\partial^2 v^*}{\partial x^{*2}} + \frac{\partial^2 v^*}{\partial y^{*2}}\right] + \left(\frac{h}{b}\right)^3 \lambda\Gamma E_y^*\left[\frac{\partial E_x^*}{\partial x^*} + \Gamma\frac{\partial E_y^*}{\partial y^*}\right] = \frac{\partial p^*}{\partial y^*}, \tag{4.20}$$

where $p^* \equiv ph^2/(\eta|\gamma_2-\gamma_1|u_0 b)$. $\lambda \equiv \epsilon\epsilon_0|\gamma_2-\gamma_1|E_0 h/(\eta\mu_0)$ is the magnitude of the electrical stress normalized to that of the viscous stress. Because the electro-osmotic mobility drives the transverse perturbations, in (4.13) and (4.20) the coefficient Γ accompanies the terms involving E_y^* and j_D^*. If electro-osmosis is suppressed then $\Gamma \ll 1$ and the transverse effects vanish.

4.3. *Component mass balances*

The solutal-component mass balances are scaled by defining

$$C_k^* \equiv \frac{C_k}{C_0|\gamma_2-\gamma_1|}, \qquad t^* \equiv \frac{t|\gamma_2-\gamma_1|u_0}{b}$$

and

$$\hat{C}_k^* \equiv \hat{C}_k/(h/b)\,Pe_k\left|\frac{1}{\gamma_2}-\frac{1}{\gamma_1}\right|C_0,$$

from which it follows that

$$\frac{\partial C_k^*}{\partial t^*} = -\left(\frac{\omega_k e}{\mu_0}\right)\frac{\partial}{\partial x^*}(\bar{z}_k E_x^* C_k^*) - \left(\frac{\Delta\omega_c}{\omega_c}\right)\left(\frac{\omega_k}{\omega_c}\right)\frac{\partial}{\partial y^*}(\bar{z}_k E_y^* C_k^*) - u^*\frac{\partial C_k^*}{\partial x^*}$$
$$-\left(\frac{h}{b}\right)Pe_k v^*\frac{\partial \hat{C}_k^*}{\partial y^*} + \left(\frac{h}{b}\right)\frac{1}{Pe_k}\frac{\partial^2 C_k^*}{\partial x^{*2}} + \frac{\partial^2 \hat{C}_k^*}{\partial y^{*2}}, \qquad k = 1, 2, \ldots, M. \quad (4.21)$$

5. Approximation for $\boldsymbol{E}(x, t)$

The development of approximate formulae for $\boldsymbol{u}$ and $\boldsymbol{E}$ begins with approximations for $\boldsymbol{E}$ because these appear in the expressions for $\boldsymbol{u}$. The electric field is governed by (4.13), which does not immediately suggest an approximate solution unless $\Gamma \ll 1$, a condition that is not generally satisfied. However, for most micro-analysis applications in microchannels and capillaries, the scaling in § 4.1 shows that $E_x \approx \langle E_x \rangle$. When combined with (4.13), this leads to an approximate solution for E_x. With the simple expression derived for E_x, E_y can then be deduced from (4.13). Several levels of approximation for E_y will be presented, each level resulting from an additional restriction that produces a simpler expression. For the sake of readability, the asterisks are hereafter dropped from the scaled variables.

5.1. *Approximation for* E_x *when* $(h/b)^2\Gamma \ll 1$, $(h/b)^3 Pe\Gamma \ll 1$

Applying the divergence theorem to (4.13) and combining the result with (4.16) leads to (Sounart 2001)

$$E_x = \frac{i_0 - \Lambda\langle i_D\rangle}{\langle\sigma\rangle} - \left(\frac{h}{b}\right)^3 Pe\Gamma\frac{\langle\hat{\sigma}\hat{E}_x\rangle}{\langle\sigma\rangle} + \left(\frac{h}{b}\right)^2\Gamma\hat{E}_x, \quad (5.1)$$

where i_0 has been scaled with $(\gamma_2/\gamma_1 - 1)^2(\gamma_1/\gamma_2)\sigma_0 E_0$. For $(h/b)^2\Gamma \ll 1$ and $(h/b)^3 Pe\Gamma \ll 1$, this yields a simple leading-order solution $E_x^{(0)}$ for E_x, viz.

$$E_x^{(0)} = \frac{i_0 - \Lambda\langle i_D\rangle}{\langle\sigma\rangle}. \quad (5.2)$$

If $\langle i_D\rangle$ and $\langle\sigma\rangle$ are replaced by i_D and σ, (5.2) is equivalent to the explicit expression obtained for E_x when E_y is identically zero (Mosher *et al.* 1992). Typically $\Lambda \ll 1$, but since it is a trivial matter to calculate the average diffusion current, $\langle i_D\rangle$ is retained here.

5.2. *Approximation for* E_y *when* $(h/b)^2\Gamma \ll 1$, $(h/b)^3 Pe\Gamma \ll 1$

Although $\boldsymbol{E}$ is nearly unidirectional for $(h/b)^2\Gamma \ll 1$ and $(h/b)^3 Pe\Gamma \ll 1$, the 'small' E_y often has an important effect on ion transport and fluid motion. The scaled component mass balances, (4.21), suggest that unless $\Delta\omega_c/\omega_c \ll O(1)$ transverse electromigration cannot be neglected, and the scaled x-momentum equation (4.19) suggests that, for $(h/b)\lambda\Gamma \geqslant O(1)$, E_y is required to calculate the electrical stresses. In other words, as for a lubrication flow, the axial electric field is calculated using the one-dimensional formulation but the transverse component is not necessarily trivial. Fortunately, the approximation $E_x \approx E_x^{(0)} \approx \langle E_x\rangle$ permits an approximate solution for E_y also. Substituting $\langle\sigma\rangle = \sigma - (h/b)Pe\hat{\sigma}$ in (4.13), integrating from zero to an arbitrary position y, combining with (5.1) and (5.2), and rearranging produces an explicit expression

for E_y, viz.

$$E_y = -\frac{1}{\sigma}\left\{ j_D + \frac{1}{\Gamma}\int_0^y \frac{\partial}{\partial x}\left[\sigma E_x^{(0)} - \left(\frac{h}{b}\right)^3 Pe\Gamma\sigma\frac{\langle\hat{\sigma}\hat{E}_x\rangle}{\langle\sigma\rangle} + \left(\frac{h}{b}\right)^2 \Gamma\sigma\hat{E}_x + \Lambda i_D\right]\mathrm{d}\xi\right\}. \tag{5.3}$$

Thus, the requirements $(h/b)^2\Gamma \ll 1$ and $(h/b)^3 Pe\Gamma \ll 1$ also permit a leading-order solution $E_y^{(0)}$ for E_y, viz.

$$E_y^{(0)} = -\frac{1}{\sigma}\left\{ j_D + \frac{1}{\Gamma}\int_0^y \frac{\partial}{\partial x}\left[\sigma E_x^{(0)} + \Lambda i_D\right]\mathrm{d}\xi\right\}. \tag{5.4}$$

If $\Lambda \ll 1$ (typical for microfluidic field strengths), this simplifies to

$$E_y^{(0)} = -\frac{1}{\sigma}\left[j_D + \frac{1}{\Gamma}\frac{\partial}{\partial x}\left(E_x^{(0)}\int_0^y \hat{\sigma}\,\mathrm{d}\xi\right)\right] \quad (\Lambda \ll 1). \tag{5.5}$$

Comparing this equation with (5.2) provides some general insight into the character of $\boldsymbol{E}$ in microfluidic systems. The applied axial electric field is relatively insensitive to the development of transverse conductivity variations (see also (4.17)) and can be calculated as a one-dimensional field using cross-sectionally averaged parameter values. The transverse component of $\boldsymbol{E}$, however, develops as a result of transverse variations in σ and E_x and thus depends on $\hat{\sigma}$; because $\hat{E}_x/E_x \ll \hat{\sigma}/\sigma$, $\hat{E}_x$ is not required to approximate E_y. Equation (5.5) is simplified further if $\Gamma \gg 1$ (high electro-osmotic mobility). Then a much simpler expression for $E_y^{(0)}$ results, viz.

$$E_y^{(0)} = -\frac{j_D}{\sigma}, \qquad \Lambda \ll 1,\ \Gamma \gg 1. \tag{5.6}$$

Finally, if $\Delta\omega_c/\omega_c \ll 1$ and $(h/b)\lambda\Gamma \ll 1$ then E_y is small enough to be neglected in the species mass balances (4.21) and the Stokes equations (4.18)–(4.20), and $\boldsymbol{E}$ can be calculated as $E_x^{(0)}(x,t)\,\boldsymbol{e}_x$.

6. Approximation for $\boldsymbol{u}(\boldsymbol{x}, t)$

Simplified expressions for $\boldsymbol{u}$ are obtained in a manner similar to that used in the preceding section to derive explicit expressions for $\boldsymbol{E}$, using the lubrication approximation $(h/b)^2 \ll 1$. As in the case of $\boldsymbol{E}$, more than one level of increasingly restrictive but simplified approximations will be presented. The solutions obtained are nearly analogous to those of other lubrication flows in thin gaps, the difference here being the inclusion of the electrical stresses.

6.1. *Approximation for u when* $(h/b)^2\Gamma \ll 1$

If $(h/b)^2 \ll 1$,† then (4.19) and (4.20) are, to leading order,

$$\frac{\partial^2 u^{(0)}}{\partial y^2} = \frac{\partial p^{(0)}}{\partial x} - \left(\frac{h}{b}\right)\lambda E_x\left[\frac{\partial E_x}{\partial x} + \Gamma\frac{\partial E_y}{\partial y}\right] \tag{6.1}$$

† It should be noted that the problem formulation in this paper begins with the Stokes equations, and therefore all computations of $\boldsymbol{u}$ (including the general simulation method of § 3) require that $(h/b)Re \ll 1$. The ratio h/b softens the low-Reynolds-number restriction for high aspect ratios; this can be shown by scaling the full Navier–Stokes equations with different axial and transverse length scales (Leal 1992).

and

$$\frac{\partial p^{(0)}}{\partial y} = \left(\frac{h}{b}\right)^3 \lambda\Gamma E_y \left[\frac{\partial E_x}{\partial x} + \Gamma \frac{\partial E_y}{\partial y}\right]. \tag{6.2}$$

Integrating (6.2) from 0 to an arbitrary position y yields an expression for the pressure, viz.

$$p^{(0)} = \left(\frac{h}{b}\right)^3 \lambda\Gamma \left[\int_0^y E_y \frac{\partial E_x}{\partial x}\,\mathrm{d}\xi + \tfrac{1}{2}\Gamma E_y^2 - p_0\right], \tag{6.3}$$

where $p_0(x,t) \equiv p^{(0)}(x,0,t)$ is an unknown parameter to be evaluated later. Substituting (6.3) into (6.1), integrating from 0 to y, and then from 1 to y yields, for $(h/b)^2 \ll 1$,

$$u^{(0)} = u_{eo} - \frac{1}{2}\frac{\partial p_0}{\partial x}(y^2 - 1) + \left(\frac{h}{b}\right)\lambda\Gamma \int_1^y \int_0^\zeta G(x,\xi,t)\,\mathrm{d}\xi\,\mathrm{d}\zeta, \tag{6.4}$$

where $u_{eo}(x,t)$ has been scaled as $(u_{eo} - U)/(u_0|\gamma_2 - \gamma_1|)$, and

$$G(x,\xi,t) \equiv \frac{\partial}{\partial x}\left[\frac{1}{2}\left(\frac{h}{b}\right)^2 \Gamma E_y^2 - \frac{1}{2\Gamma}E_x^2\right] - E_x \frac{\partial E_y}{\partial \xi}. \tag{6.5}$$

Unless the electoosmotic mobility is unusually high $\Gamma \leqslant O(1)$, so if $(h/b)^2 \ll 1$ then G typically reduces to

$$G = -E_x \frac{\partial E_y}{\partial y} - \frac{1}{2\Gamma}\frac{\partial E_x^2}{\partial x}; \tag{6.6}$$

$\partial p_0/\partial x$ is evaluated by recognizing that $\langle u^{(0)}\rangle = 0$. Solving for $\partial p_0/\partial x$ by integrating (6.4) over y from 0 to 1, setting the left-hand side equal to zero, combining with (6.4) and (6.6), and simplifying gives (Sounart 2001)

$$u^{(0)} = u_{eo} + \frac{3}{2}\left[u_{eo} - \left(\frac{h}{b}\right)\lambda\Gamma E_x \int_0^1 \int_1^y E_y\,\mathrm{d}\xi\,\mathrm{d}y\right](y^2 - 1) - \left(\frac{h}{b}\right)\lambda\Gamma E_x \int_1^y E_y\,\mathrm{d}\xi. \tag{6.7}$$

Here u_{eo} and the electric field are evaluated in terms of the ion distributions, as described in § 5. To leading order, then, the axial velocity distribution can be calculated directly if the ion concentration field is known.

6.2. *Approximation for v and Ψ when $(h/b)^2\Gamma \ll 1$*

The transverse velocity component follows from continuity, viz.

$$v = -\int_0^y \frac{\partial u}{\partial x}\,\mathrm{d}\xi. \tag{6.8}$$

Substituting $u^{(0)}$ from (6.7) for u in (6.8) and carrying out the integration yields a leading-order expression for v, viz.

$$v^{(0)} = \tfrac{1}{2}(y - y^3)\frac{\partial u_{eo}}{\partial x} + \tfrac{1}{2}(y^3 - 3y)\left(\frac{h}{b}\right)\lambda\Gamma \frac{\partial}{\partial x}\left[E_x \int_0^1 \int_1^y E_y\,\mathrm{d}\xi\,\mathrm{d}y\right] + \left(\frac{h}{b}\right)\lambda\Gamma \frac{\partial}{\partial x}\left[E_x \int_0^y \int_1^y E_y\,\mathrm{d}\xi\,\mathrm{d}y\right]. \tag{6.9}$$

The stream function (scaled with $u_0|\gamma_2 - \gamma_1|h$) is calculated similarly as $\psi = \int_0^y u \, d\xi$, which to leading order is

$$\psi^{(0)} = \tfrac{1}{2}(y^3 - y)u_{eo} - \tfrac{1}{2}(y^3 - 3y)\left(\frac{h}{b}\right)\lambda\Gamma E_x \int_0^1 \int_1^y E_y \, d\xi \, dy - \left(\frac{h}{b}\right)\lambda\Gamma E_x \int_0^y \int_1^y E_y \, d\xi \, dy. \quad (6.10)$$

6.3. *Electrical stresses negligible, i.e.* $(h/b)\lambda\Gamma \ll 1$

If $(h/b)\lambda\Gamma \ll 1$ then the electrical stresses are negligible and $u^{(0)}$, $v^{(0)}$, and $\psi^{(0)}$ are calculated, respectively, as

$$u^{(0)} = u_{eo} + \tfrac{3}{2}u_{eo}(y^2 - 1), \qquad (h/b)\lambda\Gamma \ll 1, \quad (6.11)$$

$$v^{*(0)} = \tfrac{1}{2}(y - y^3)\frac{\partial u_{eo}}{\partial x}, \qquad (h/b)\lambda\Gamma \ll 1, \quad (6.12)$$

$$\psi^{(0)} = \tfrac{1}{2}(y^3 - y)u_{eo}, \qquad (h/b)\lambda\Gamma \ll 1. \quad (6.13)$$

7. Approximation summary

Equations (5.2), (5.4), (6.7), (6.9), and (6.10) provide explicit solutions for $\boldsymbol{E}$, $\boldsymbol{u}$, and ψ in an arbitrary electrolyte-filled two-dimensional channel as long as $(h/b)^2\Gamma \ll 1$ and $(h/b)^3 Pe\Gamma \ll 1$. Γ is a ratio of mobilities that is virtually always $O(1)$ or less, so the essential requirement for these simplifications is that the ratio of the characteristic transverse and axial length scales must be small; specifically, $(h/b)^2 \ll 1$ and $(h/b)^3 \ll 1/Pe$. Further truncation of these equations is also possible for more restrictive cases delineated by the non-dimensional groups in the formulae. Successive approximations for E_y are given by (5.5) and (5.6), and greatly simplified expressions, (6.11)–(6.13), are obtained for $\boldsymbol{u}$ and ψ when the electrical stresses are negligible, i.e. $(h/b)\lambda\Gamma \ll 1$.

There are many similarities between the approximations for $\boldsymbol{E}$ and $\boldsymbol{u}$. The critical approximation that leads to all the simplified expressions is that each of these fields is nearly unidirectional, which for both fields requires that $(h/b)^2\Gamma \ll 1$. When the electrical stresses are negligible in the Stokes equations, the axial component of $\boldsymbol{u}$, as well as $\boldsymbol{E}$, is calculated as a quasi-one-dimensional field. Then, once the simple algebraic solutions for the axial components are obtained, the transverse components of $\boldsymbol{E}$ and $\boldsymbol{u}$ are rendered from the two-dimensional charge balance and continuity equation, respectively. Inclusion of the electrical stresses in the momentum balance simply results in additional, albeit more complicated, terms in the explicit expressions for $\boldsymbol{u}$ that provide additional coupling to $\boldsymbol{E}$.

The approximate theory has been derived generally for an arbitrary conductivity gradient in a rectilinear channel with a thin double layer. It is therefore applicable to any electrolyte system as long as $\kappa h \gg 1$ and all gradients are sufficiently gradual relative to the channel width. The model may therefore be applied to typical IEF, ITP, FASS, high-ionic-strength electro-osmotic pumping, and other common microfluidic separation and transport schemes. In the following section, the model will be demonstrated and evaluated by applying it to a sample stacking and electro-osmotic pumping configuration.

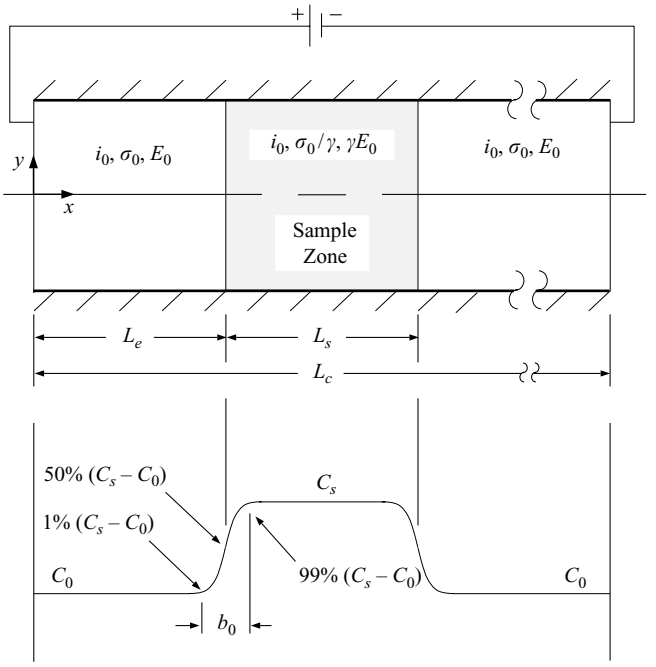

FIGURE 2. The prototype system configuration and initial conditions. The concentration field shown applies to buffer components for $\gamma < 1$. For $\gamma > 1$, C_s is less than C_0. Because of the high aspect ratio, the diagram is not drawn to scale.

8. Application to stacking and pumping buffers

To evaluate the approximations, a prototype non-uniform buffer configuration examined previously (Sounart & Baygents 2001) and illustrated in figure 2, was simulated by the numerical solution presented in § 3. This numerical solution was then compared with the results obtained using the semi-analytic expressions derived for $\boldsymbol{E}$ and $\boldsymbol{u}$ in § 5 and § 6. In all test cases, the initial concentration fields were cross-sectionally uniform, and sigmoidal zone boundaries were initialized with width b_0. The evaluation begins in § 8.1 with a simulation of the high-ionic-strength electro-osmotic pumping problem discussed in Sounart & Baygents (2001) ($h/b_0 = 1/6$), but with $\gamma = 1/10$ rather than $1/5$; γ is the field amplification factor defined by Burgi & Chien (1991) as the ratio of the electric field in the stacking sample zone and that in the buffer outside the sample zone (so for this configuration $\gamma_1 = \gamma$ and $\gamma_2 = 1$). Because $\Delta\omega_c/\omega_c \ll 1$ for this buffer, E_y is not calculated. The initial fluid-velocity field is first examined in detail and shown to be accurately captured using the approximations. It is then demonstrated that during the transport of the high-conductivity zone, significant errors are introduced temporarily over a small part of the zone boundary, because of a transient sharpening of the conductivity gradient in that region. The error is short-lived and affects only a small section of the transition region. The pumping configuration is modified in § 8.2 by reducing the initial zone-boundary length in such a way that $h/b_0 = 2$. It is shown that although the lubrication approximation for $\boldsymbol{u}$ yields a poor representation of the initial velocity field, dispersion rapidly reduces h/b_0 and the approximation error quickly decays to that for $h/b_0 = 1/6$. The approximations are shown to predict accurately the field variables at $t = 2$ (i.e. two characteristic times for convection across the sample zone).

E_0 (V cm^{-1})	Buffer	γ $\frac{E_{x,s}}{E_0}$	Re $\frac{\rho u_0 \lvert \gamma_2 - \gamma_1 \rvert h}{\eta}$	Pe $\frac{\lvert \gamma_2 - \gamma_1 \rvert u_0 h}{\omega_k k_B T}$	λ $\frac{\epsilon\epsilon_0 \lvert \gamma_2 - \gamma_1 \rvert E_0 h}{\eta \mu_0}$	Γ $\frac{\mu_0}{\omega_c e}$	Λ $\frac{k_B T/e}{\lvert \gamma_2 - \gamma_1 \rvert E_0 b}$
180	A	1/10	0.014	24	5.0	0.08	10^{-4}
		1/10	0.022	21	3.3	0.82	10^{-3}
		1/50	0.024	23	3.6	0.82	10^{-3}
	B	2	0.025	23	3.6	0.82	10^{-3}
		5	0.099	93	14.6	0.82	10^{-4}
720	B	2	0.099	93	14.6	0.82	10^{-4}

TABLE 1. Dimensionless groups for 2-D simulations. The formula for each quantity is given under the corresponding symbol in the column headings. $E_{x,s}$ is the value of E_x in the sample zone. $h/L_s = 0.02$ for all simulations; ρ is the fluid density. The definitions listed for Γ and Λ assume the usual case, $\Delta\omega_c \sim \omega_c$; for the special case $\Delta\omega_c \ll \omega_c$ (buffer A), the quantities listed for the definition must be multiplied by $\Delta\omega_c/\omega_c$. For the prototype buffer configuration, $\gamma_1 = 1$ and $\gamma_2 = \gamma$.

In § 8.3, electro-osmotic pumping is simulated with another buffer, buffer B, for which $\Delta\omega_c/\omega_c \sim O(1)$. It is first shown that if E_y is not calculated then ion transport is not as well captured for this buffer. The approximations for E_y from (5.4) and (5.6) are then compared, and their inclusion in the problem formulation is shown to improve the solutions for σ and $\boldsymbol{u}$ at $\gamma = 1/10$. The results are also compared for $\gamma = 1/50$, and it is shown that approximation errors are insignificant and decay after a transient growth. The more general formula (5.4) for E_y is shown to reduce approximation errors substantially for $\gamma = 1/10$ and $1/50$.

The semi-analytic expressions for $\boldsymbol{u}$ and $\boldsymbol{E}$ are evaluated for $\gamma > 1$ in § 8.4. Approximation errors are shown to be small for $\gamma = 2$, particularly if E_y is computed using (5.4). For $\gamma = 5$, it is shown that the electrical stresses alter the character of the flow, but only transiently, and the simple approximations (6.11)–(6.13) that neglect these stresses are effective after the transient. A final evaluation is then made for a flow that is significantly affected by the electrical stresses and can be characterized using (6.7), (6.9), and (6.10). The fidelity of these approximations is demonstrated by increasing the electric field at $\gamma = 2$ by a factor 4.

Values of the non-dimensional groups for each set of initial buffer conditions are provided in table 1. The zone-boundary length b changes with time, so b equals b_0 only at the outset, when all fields are cross-sectionally uniform. Recall that the scaling arguments in the charge balance only apply for $t > h^2/(\omega_c k_B T)$, at which time simulation results have shown that b has spread to $O(L_s)$. As a result, $b = L_s$ is used for all dimensionless parameters that depend on b, including Λ and h/b in table 1. For all buffer configurations in this paper, E_x was calculated from (5.2).

8.1. $\gamma < 1$, *buffer A* ($\Delta\omega_c/\omega_c \ll 1$) *when* $(h/b_0)^2 \ll 1$

The approximations were first tested by simulating electro-osmotic pumping at $\gamma = 1/10$ using the buffer studied in Sounart & Baygents (2001), which will henceforth be referred to as buffer A. The running buffer consisted of 100 mM Tris base and 200 mM cacodylic acid (pH = 6.2, $\sigma_0 = 0.452$ S m^{-1}). The geometric lengths of the system were $L_e = L_s = 1$ mm, $h = 20\,\mu$m, and $L_c = 5$ cm. A constant current was maintained by requiring $i_0 = 8$ kA m^{-2} in the running buffer, corresponding to $E_0 = 180$ V cm^{-1}; $b_0/L_s = 0.12$, so $h/b_0 = 1/6$. For the approximate solutions, (6.11)–(6.13)

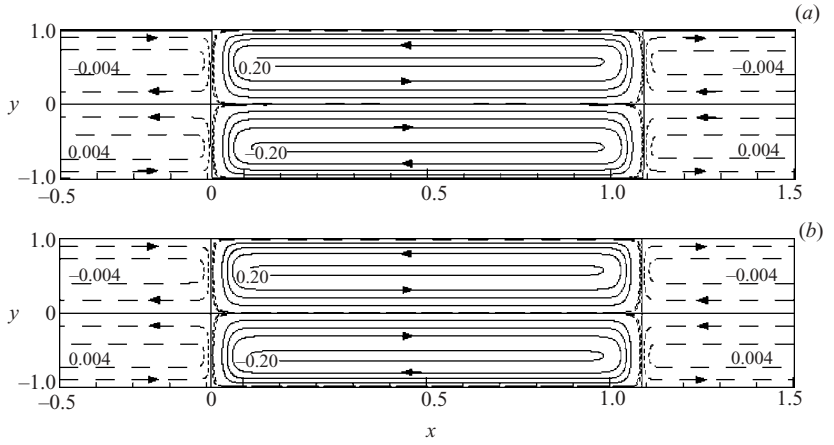

FIGURE 3. Initial streamlines for buffer A, $\gamma = 1/10$, computed by (*a*) numerical solution and (*b*) the lubrication approximation, (5.2), (6.11), (6.12), (6.13), and $E_y = 0$. The solid lines represent contours of constant ψ from –0.2 to 0.2 at intervals of 0.05; the dashed lines represent the same from −0.004 to 0.004 at intervals of 0.002. The ratio $h/b_0 = 1/6$. Running buffer: 200 mM cacodylic acid, 100 mM Tris; $\sigma_0 = 0.45\,\mathrm{S\,m^{-1}}$, $E_0 = 180\,\mathrm{V\,cm^{-1}}$, $i_0 = 8\,\mathrm{kA\,m^{-2}}$, $u_0 = 0.8\,\mathrm{mm\,s^{-1}}$, pH = 6.2. $L_s = 1$ mm, $L_c = 5$ cm, $h = 20\,\mu$m.

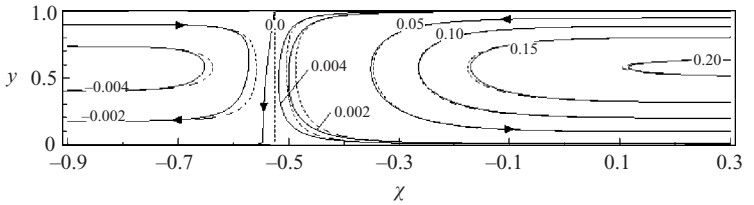

FIGURE 4. Initial streamlines in the upstream zone boundary calculated by complete numerical solution (solid lines) and approximate solution (dashed lines). The value of ψ is given for each contour. χ is x rescaled on b_0. The simulation conditions and approximations are as in figure 3.

were used to calculate u, v, and ψ. Tris base and cacodylic acid have approximately the same mobility, $\Delta\omega_c/\omega_c \ll 1$, and so E_y was not calculated.

Initial streamlines in the moving reference frame are shown in figure 3. The circulation patterns are similar in form to those reported by Anderson and Idol for a harmonic zeta-potential distribution (cf. figure 2 of Anderson & Idol 1985), but here the two-dimensional velocity field is confined to the initially sharp zone-boundary regions, and there is no antisymmetry in x about the stagnation streamline (because E_x is nonlinear in σ). Since the initial electric field is identically unidirectional, initial approximation errors result only from the lubrication approximation used to calculate $\boldsymbol{u}$. The streamlines obtained using the approximations are indistinguishable, on the sample-zone length scale, from those obtained with the complete numerical solution. Figure 4 focuses on the streamlines in the upstream zone boundary. The approximate streamlines (dashed) deviate slightly from those calculated numerically (solid), primarily near the stagnation streamline. The lubrication approximation is least accurate in this region because u changes over a smaller length scale than b. This results from the nonlinear relationship between E_x and σ, viz.

$$E_x \sim \frac{i_0}{\sigma} \qquad \Rightarrow \qquad \frac{\delta E_x}{\delta \sigma} \sim \frac{i_0}{\sigma^2}, \tag{8.1}$$

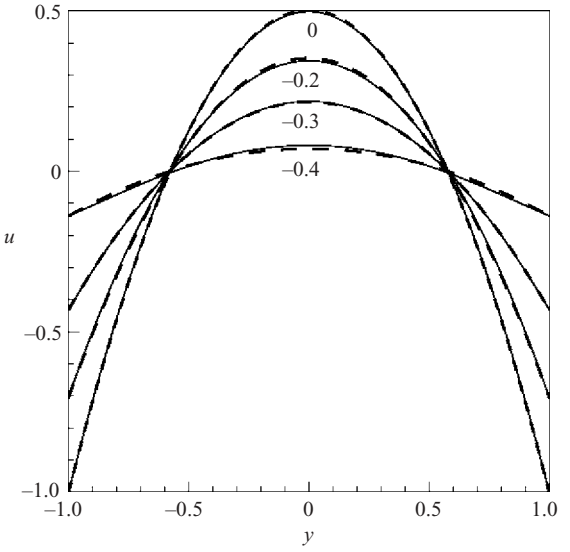

FIGURE 5. Initial axial-velocity profiles in the upstream zone boundary, at selected values of χ. Solid line, complete numerical solution; dashed line, approximate solution. The simulation conditions and approximations are as for figure 3.

which implies that b (the characteristic axial length scale for σ) is not necessarily the characteristic axial length scale for E_x, or consequently for u, over the entire zone boundary. A more general axial length scale b' for variations of E_x and u is derived as follows. Since $\delta E_x/\delta x \sim |\gamma - 1|E_0/b'$ implies that

$$b' \sim \frac{|\gamma - 1|E_0}{(\delta E_x/\delta\sigma)(\delta\sigma/\delta x)} \tag{8.2}$$

and $\delta\sigma/\delta x \sim |\gamma - 1|\sigma_0/b\gamma$ then using (8.1),

$$b' \sim \gamma \left(\frac{\sigma}{\sigma_0}\right)^2 b. \tag{8.3}$$

So, as σ ranges from σ_0 to σ_0/γ in the transition from running buffer to sample zone, b' ranges from γb to b/γ, respectively, i.e.

$$b' = b/\alpha, \qquad \alpha \equiv \begin{cases} \gamma, & \text{inner region } (\sigma \sim \sigma_0/\gamma), \\ 1/\gamma, & \text{outer region } (\sigma \sim \sigma_0). \end{cases} \tag{8.4}$$

Thus $b' \sim b$ throughout the boundary zone only for $\gamma = O(1)$. For $\gamma \gg 1$ or $\gamma \ll 1$, the scaling in §4 applies to the region of the zone boundary where $b' \sim b$, i.e. where $\sigma/\sigma_0 \sim 1/\sqrt{\gamma}$. Near the stagnation streamline $\sigma \sim \sigma_0$, so $\alpha = 1/\gamma$ and $b' = \gamma b = b/10$. Thus near the stagnation streamline, E_x and u change locally on an order-of-magnitude smaller length scale than σ, so the lubrication approximation is less accurate.

It is important to note that the ψ contours are given in increments of 0.002 where the most significant errors are observed; increments of 0.05 are given in the region where better agreement is obtained. Since the fluid-velocity components are given by spatial derivitives of ψ, this shows that the relative error in the velocity field is only significant where the fluid velocity approaches zero. Figure 5 shows initial

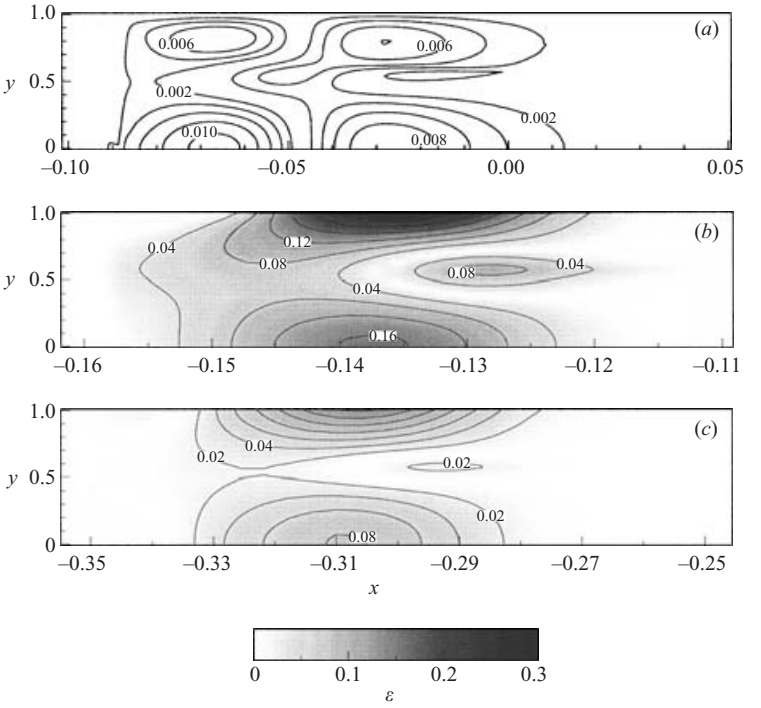

FIGURE 6. Fluid-speed approximation error ε in the upstream zone boundary, at (*a*) $t = 0$, (*b*) $t = 0.4$, and (*c*) $t = 2$. The solid lines represent contours of constant ε, from 0.002 to 0.01 at intervals of 0.002 ($t = 0$), from 0.04 to 0.28 at intervals of 0.04 ($t = 0.4$), and from 0.02 to 0.14 at intervals of 0.02 ($t = 2$). The simulation conditions and approximations are as for figure 3.

axial-velocity profiles in the upstream zone boundary. The profiles have a parabolic form throughout the zone boundary and are essentially equivalent to those given by the lubrication approximation.

The zone boundaries are ultimately distorted by the fluid motion and electrodiffusional transport, causing the conductivity, electric, fluid-velocity, and component-concentration fields to evolve in time. Figure 6 shows the magnitude of the error in the fluid speed $\varepsilon \equiv | |\boldsymbol{u}^{(0)}| - |\boldsymbol{u}| |$ after 0, 0.4, and 2 characteristic times for convection across the sample zone. The approximation error increases substantially over a small part of the zone boundary (note the plot scales and see figure 7) by $t = 0.4$, but then decreases by $t = 2$. The error develops because of the nonlinearity in the zone boundary (discussed above) and is compounded by a transient increase in the conductivity gradient over part of the channel cross-section. Figure 7 shows that when $t = 0.4$ the conductivity gradient near the wall, in the low-conductivity region of the zone boundary, is greater than at $t = 0$. By a mechanism analogous to that of zone-boundary sharpening in isotachophoretic separations (Mosher *et al.* 1992), this sharpening occurs initially where $\partial u/\partial x < 0$ because, for this condition, the fluid upstream moves faster than the fluid downstream, which creates a net convective flux opposite to that driven by diffusion. Notice in figure 3 that there are six stagnation points, three on each side of the low-conductivity zone. In the upstream boundary, the fluid moves axially toward the two stagnation points at the channel wall and transversely away from them, and vice versa for the stagnation point at

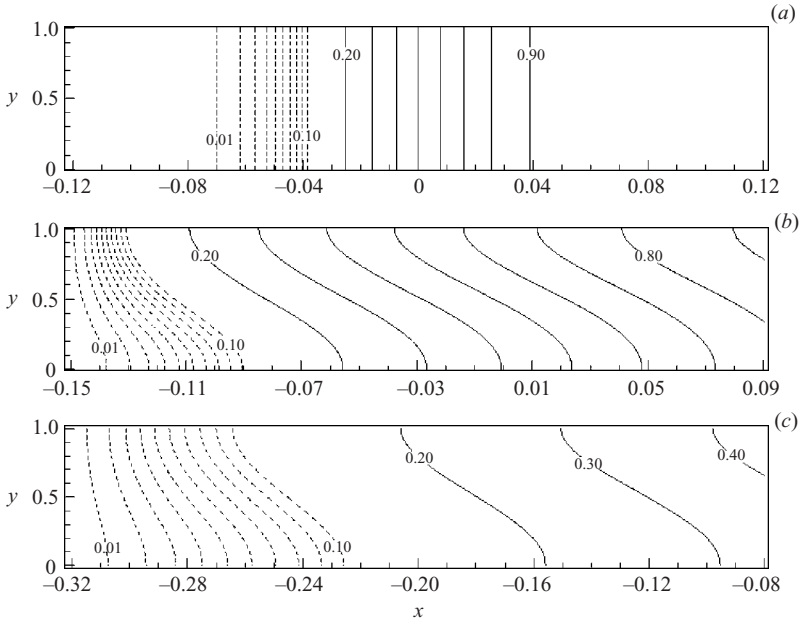

FIGURE 7. Conductivity field in the upstream zone boundary calculated by complete numerical solution, at (*a*) $t = 0$, (*b*) $t = 0.4$, and (*c*) $t = 2$. The solid lines represent contours of constant $\sigma - 1/(1/\gamma - 1)$ from 0.2 to 0.9 at intervals of 0.1; the dashed lines represent contours of the same quantity from 0.01 to 0.1 at intervals of 0.01. The simulation conditions are as for figure 3.

the centreline. Initially the y-component of the conductivity gradient vanishes, so where the fluid moves axially toward the stagnation point the gradient is compressed, and where it moves away the gradient is stretched, such as at the centreline in the upstream boundary (cf. figure 7*b*). This creates a two-dimensional conductivity field, and cross-sectional diffusion ultimately transfers the spreading at the centreline to the channel wall, eliminating the local, transient, focusing of the electrolyte zone boundary (figure 7*c*). The transient sharpening of the conductivity gradient decreases the local transition length for the electric field and thus the electro-osmotic slip velocity, as shown in figure 8. The characteristic length for velocity changes approaches h in this region where $| \partial u_{eo}/\partial x |$ is the greatest, and there the lubrication approximations fail. This process affects only a short segment along the wall and has most impact where the flow is weakest. Also, diffusion eventually reduces the conductivity and velocity gradients (figures 7 and 8), and the error diminishes (figure 6) by $t = 2$. Thus the error in the lubrication approximation is both short-lived and confined to a small portion of the domain.

8.2. $\gamma < 1$, *buffer A* ($\Delta\omega_c/\omega_c \ll 1$) *when* $h/b_0 = O(1)$

Since the zone-boundary length in the previous configuration was initialized somewhat arbitrarily, the simulation was repeated with $h/b_0 = 2$. A zone boundary of approximately this length would result within 50 ms, given only diffusion as a dispersion mechanism. Initial streamlines and axial-velocity profiles near the upstream zone boundary are shown in figures 9 and 10, respectively. Clearly the lubrication approximation does not accurately capture the initial fluid-velocity field. The lubrication

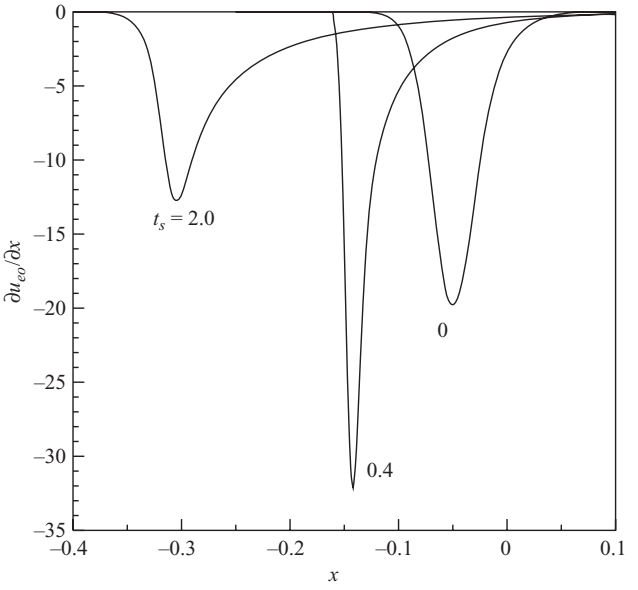

FIGURE 8. Axial derivative of the slip velocity in the upstream zone boundary, calculated by complete numerical solution, at selected values of t. The simulation conditions are as for figure 3.

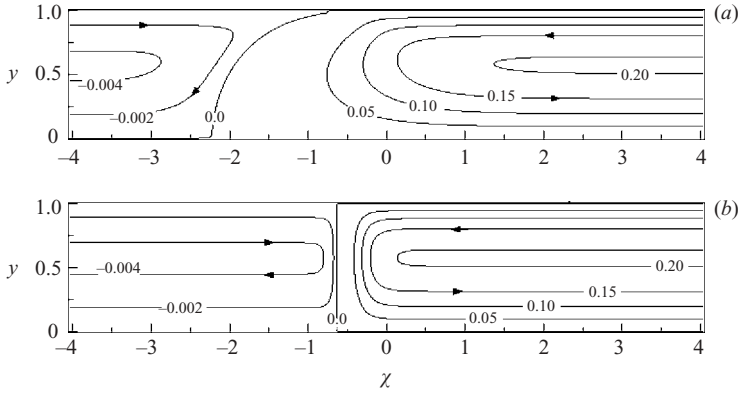

FIGURE 9. Initial streamlines in the upstream zone boundary, computed by (*a*) numerical solution and (*b*) the lubrication approximation. The value of ψ is given for each contour. The ratio $h/b_0 = 2$; all other simulation conditions and approximations are as for figure 3.

approximation yields streamlines of the form reported in figure 2 of Anderson & Idol (1985), but the numerical solution shows streamlines of a different shape. Also, the axial-velocity profiles are not parabolic in the zone boundary as predicted by the lubrication approximation, and the region of two-dimensional fluid motion extends beyond the zone boundary. However, the zone boundary rapidly spreads, so that $(h/b)^2 \ll 1$ within fractions of a second ($t < 1$). Figure 11 shows the maximum and average ε (ε_{max} and ε_{avg}) in the zone boundaries for $h/b_0 = 2$ and $h/b_0 = 1/6$. As discussed previously, for $h/b_0 = 1/6$ the error increases initially and then decays as the zone boundaries spread. For $h/b_0 = 2$, ε is initially as high as 0.8 but decays immediately and ultimately follows a course nearly identical to that for $h/b_0 = 1/6$.

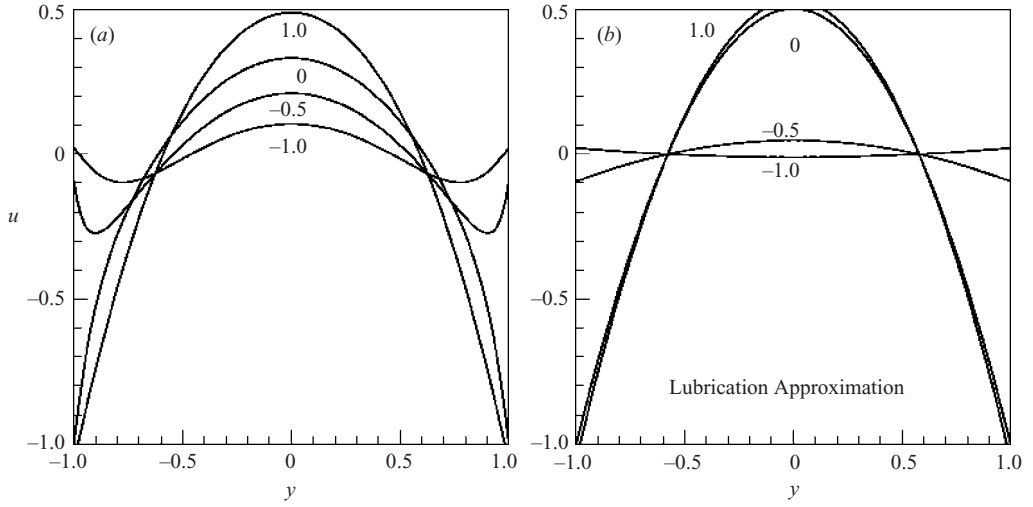

FIGURE 10. Initial axial-velocity profiles in the upstream zone boundary, at selected values of χ. (*a*) Numerical solution, (*b*) lubrication approximation. The simulation conditions and approximations are as for figure 9.

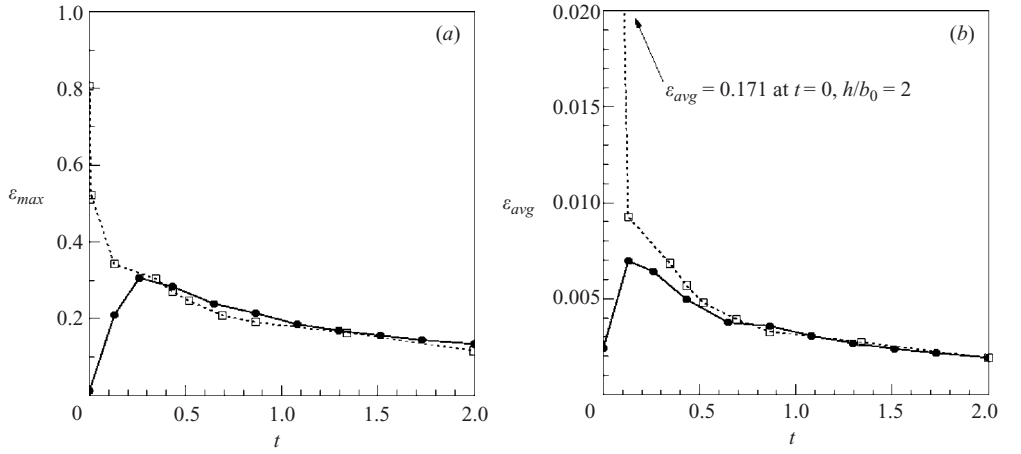

FIGURE 11. Time dependence of the fluid-speed approximation error for $h/b_0 = 1/6$ (solid lines) and $h/b_0 = 2$ (dotted lines). Simulation conditions and approximations are as for figure 3. (*a*) ε_{max}, (*b*) ε_{avg}.

This occurs because, for $t > 0.5$, σ, $\boldsymbol{u}$, and $\boldsymbol{E}$ are approximately the same for any $h/b_0 \geqslant 1/6$; i.e. the system is insensitive to the initial zone-boundary length, at least for $h/b_0 \geqslant 1/6$.

Streamlines and contours of constant conductivity and electric potential in both zone boundaries are shown in figure 12 at $t = 2$. The approximate and numerical solutions are in substantial agreement over most of the transition from running buffer to sample zone. The transverse conductivity gradients are caused by the electrolyte motion, and despite this, the potential contours show the electric field is virtually unidirectional. Such results are consistent with the scaling arguments

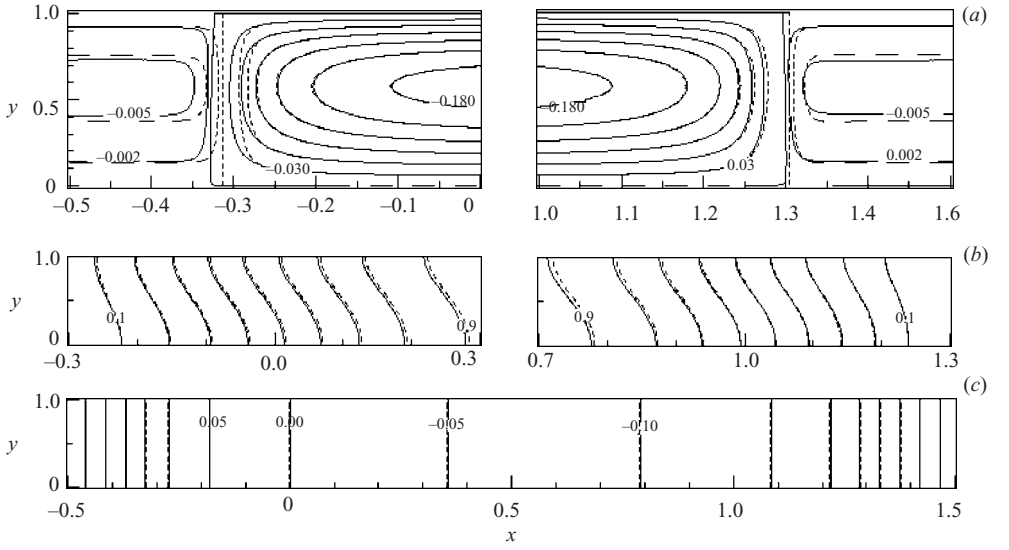

FIGURE 12. (*a*) Streamlines, (*b*) conductivity contours and (*c*) potential contours at $t = 2$. Solid lines, complete numerical solution; dashed lines, approximate solution. The unlabelled streamlines in the top panel are shown for ψ from 0.06 to 0.15 at intervals of 0.03; values of ψ are given for all other streamlines. Conductivity contours are shown for $\sigma - 1/(1/\gamma - 1)$ from 0.1 to 0.9 at intervals of 0.1; potential contours are shown for $[\phi - \phi(x = 0)]/(E_0|\gamma - 1|L_s)$ from -0.45 to 0.30 at intervals of 0.05. The simulation conditions and approximations are as for figure 9.

(cf. (4.8) and (4.16)), which suggest that transverse variations in σ and E_x should be $O[(h/b)Pe] \sim O(10^{-1})$, and $O[(h/b)^2\Gamma] \sim O(10^{-5})$, respectively.

8.3. $\gamma < 1$, *buffer B* ($\Delta\omega_c/\omega_c \sim 1$)

Electro-osmotic pumping at $\gamma = 1/10$ was simulated with another buffer, buffer B, to demonstrate that the approximations are not limited to a parameter space with $\Delta\omega_c/\omega_c \ll 1$. The running buffer consisted of 20 mM ACES and 9 mM NaOH (pH = 6.2, $\sigma_0 = 0.0723\,\mathrm{S\,m^{-1}}$) (Thormann *et al.* 1998). All other simulation conditions were equivalent to those in § 8.1. If E_y is not calculated, the ion transport is not predicted as accurately as for buffer A, as can be seen in the conductivity contours shown in figure 13(*a*). E_y is more important for buffer B because $\Delta\omega_c/\omega_c \sim 1$ (cf. (4.21)). This is clear from figure 13(*b*), which shows that the approximate conductivity contours match the complete numerical solution at least as well as for buffer A when the mobility of ACES is artificially changed to equal that of NaOH.

The approximation can be improved significantly for buffer B by calculating E_y using (5.4) or (5.5) or even the simple expression in (5.6). Figure 14 shows approximate E_y contours calculated from (5.4) and (5.6) for comparison with those computed from the complete numerical solution. Although $\Gamma \sim 1$, (5.6) provides a reasonable approximation to E_y in the inner region of the zone boundary but fails in the outer region, where the integral in (5.4) becomes important. The slightly more complicated expression in (5.4) greatly improves the estimate of E_y throughout both zone boundaries and has an insignificant effect on the simulation time.

To understand why (5.6) produces a good approximation for E_y in the inner region, the deviations from the scaling in § 4 must be considered. Since E_x changes by $O(1)$

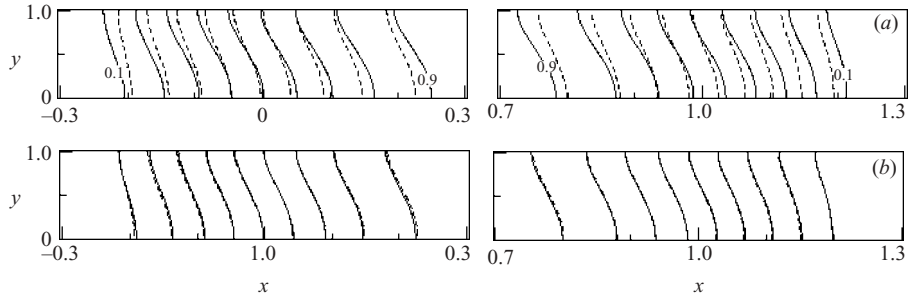

FIGURE 13. Conductivity contours at $t = 2$ for $\gamma = 1/10$, calculated by complete numerical solution (solid lines) and approximately (dashed lines). (*a*) Buffer B, (*b*) buffer B with ω_{ACES} set equal to ω_{Na^+}. Contours are shown for $\sigma - 1/(1/\gamma - 1)$ from 0.1 to 0.9 at intervals of 0.1. Running buffer, 20 mM ACES, 9 mM NaOH; $\sigma_0 = 0.072\,\mathrm{S\,m^{-1}}$, $E_0 = 180\,\mathrm{V\,cm^{-1}}$, $i_0 = 1.3\,\mathrm{kA\,m^{-2}}$, $u^0_{eo} = 1.2\,\mathrm{mm\,s^{-1}}$, pH = 6.2. $L_s = 1\,\mathrm{mm}$, $L_c = 5\,\mathrm{cm}$, $h = 20\,\mu\mathrm{m}$. The approximate solution was calculated from (5.2), (6.11), (6.12), (6.13), and $E_y = 0$.

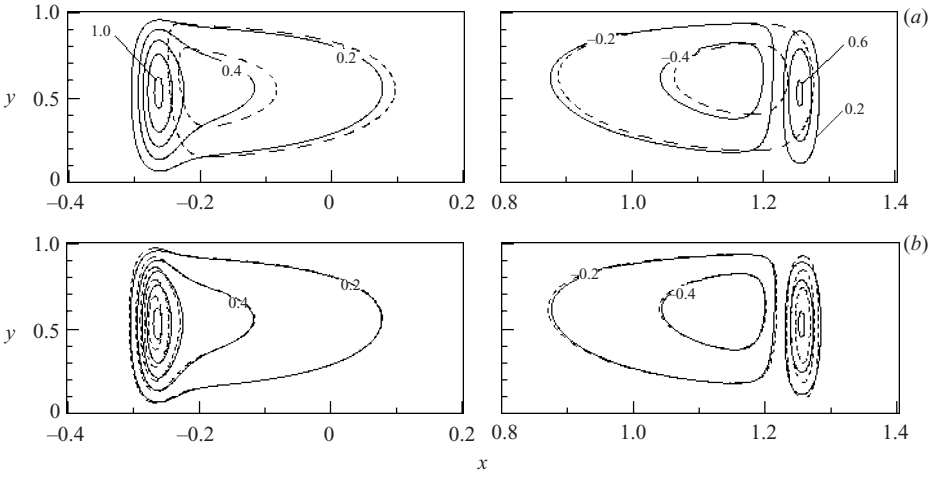

FIGURE 14. E_y contours for buffer B, $\gamma = 1/10$ at $t = 2$, calculated by complete numerical solution (solid lines) and approximately (dashed lines). The approximate E_y contours are from (*a*) (5.6) and (*b*) (5.4). All other approximations are as for figure 13. The contours are shown for E_y from -0.4 to 1.0 at intervals of 0.2. The simulation conditions are as for figure 13.

over the length scale b/α (cf. (8.4)), (5.5) can be written more generally if x is rescaled with b/α, whence it reads

$$E_y^{(0)} = -\frac{1}{\sigma}\left[j_D + \frac{\alpha}{\Gamma}\frac{\partial}{\partial x}\left(E_x^{(0)}\int_0^y \hat{\sigma}\,\mathrm{d}\xi\right)\right]. \tag{8.5}$$

Thus the integral in (8.5) is approximately an order of magnitude less than j_D in the inner region ($\alpha = \gamma = 1/10$), which extends from $\sigma = \sigma_0/\gamma$ to $\sigma_0/\sqrt{\gamma}$, and does not significantly affect the calculation of E_y over approximately two-thirds of the zone boundary. In the outer region, where $\alpha = 1/\gamma = 10$, the integral is important and the calculation of E_y from (5.6) is a poor approximation.

Figures 15 and 16 show the conductivity contours and streamlines, respectively, at $t = 2$, calculated using all three approximations for E_y. Equations (5.4) and (5.6)

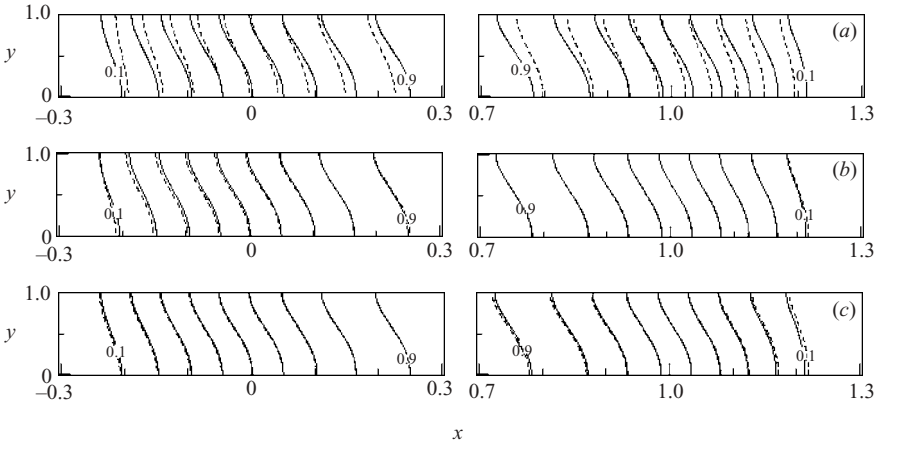

FIGURE 15. Conductivity contours for buffer B, $\gamma = 1/10$ at $t = 2$, calculated by complete numerical solution (solid lines) and approximately (dashed lines). The approximate E_y contours are from (*a*) $E_y = 0$, (*b*) (5.6), and (*c*) (5.4). All other approximations are as for figure 13. Contours are shown for $\sigma - 1/(1/\gamma - 1)$ from 0.1 to 0.9 at intervals of 0.1. The simulation conditions are as for figure 13.

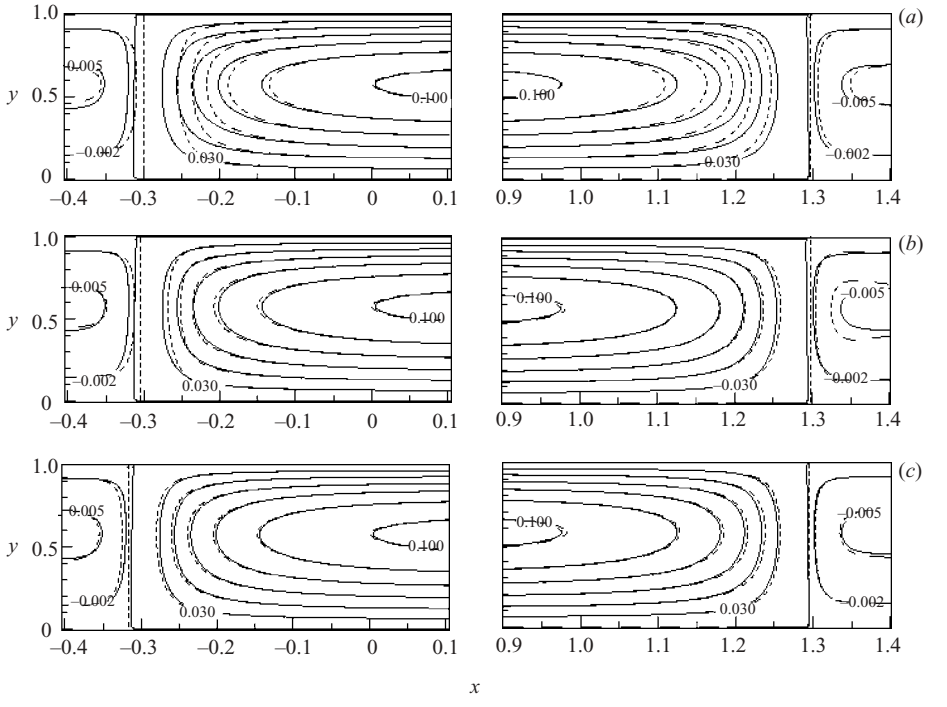

FIGURE 16. Streamlines for buffer B, $\gamma = 1/10$ at $t = 2$, calculated by complete numerical solution (solid lines) and approximately (dashed lines). The approximate E_y contours are from (*a*) $E_y = 0$, (*b*) (5.6), and (*c*) (5.4). All other approximations are as for figure 13. Unlabelled streamlines are shown for ψ from 0.06 to 0.15 at intervals of 0.03. The simulation conditions are as for figure 13.

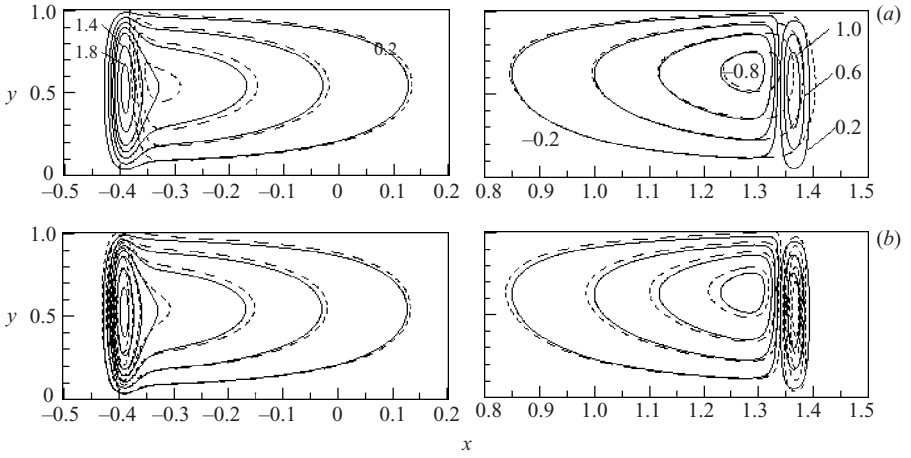

FIGURE 17. E_y contours for buffer B, $\gamma = 1/50$ at $t = 2$, calculated by complete numerical solution (solid lines) and approximately (dashed lines). The approximate E_y contours are from (*a*) (5.6) and (*b*) (5.4). All other simulation conditions and approximations are as for figure 13. Contours are shown for E_y in the upstream boundary from 0.2 to 1.0 at intervals of 0.2 and also for 1.4, 1.8 and in the downstream boundary from −0.2 to −0.8 at intervals of 0.2 and from 0.2 to 1.0 at intervals of 0.4.

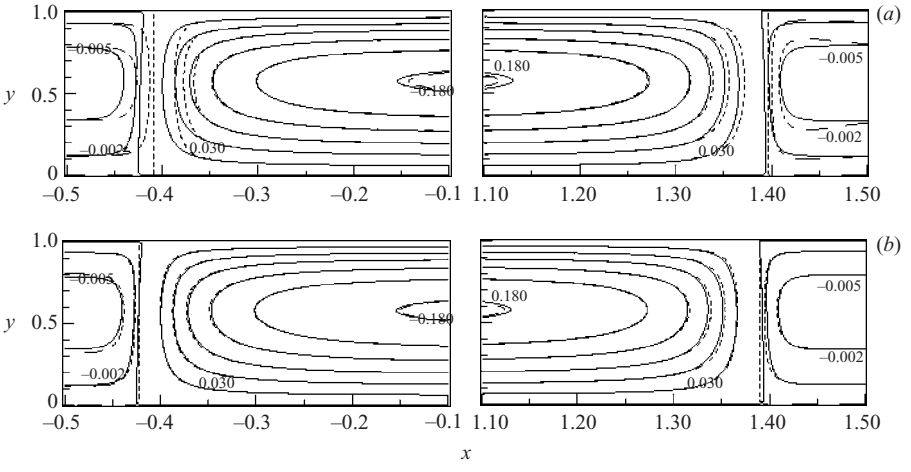

FIGURE 18. Streamlines for buffer B, $\gamma = 1/50$ at $t = 2$, calculated by complete numerical solution (solid lines) and approximately (dashed lines). The approximate E_y contours are from (*a*) (5.6) and (*b*) (5.4). All other simulation conditions and approximations are as for figure 13. Unlabelled streamlines are shown for ψ from 0.06 to 0.15 at intervals of 0.03.

substantially improve the approximations. Equation (5.4) only slightly improves the approximation of the streamlines in the outer region over the approximation provided by (5.6), because much of the residual error in this region results from use of the lubrication approximation for the fluid motion.

Similar results are obtained for $\gamma = 1/50$, as shown in figures 17 and 18. The more accurate approximation of E_y in the outer region provided by (5.4) has a more important effect on the streamlines at $\gamma = 1/50$ because α is a factor 5 larger. The accuracy of the approximations for the electro-osmotic pumping configuration with

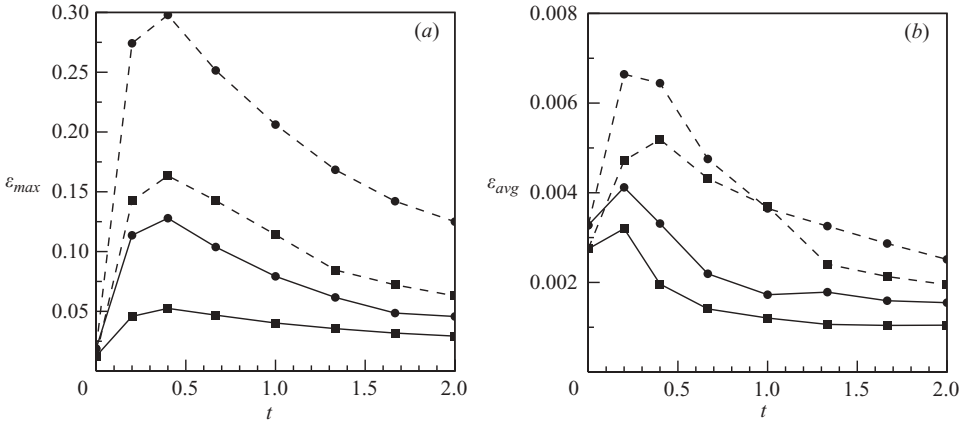

FIGURE 19. Time dependence of the fluid-speed approximation error for buffer B, $\gamma < 1$. E_y was calculated from (5.4) (solid lines) and (5.6) (dashed lines); ■, $\gamma = 1/10$; ●, $\gamma = 1/50$. All other simulation conditions and approximations are as for figure 13. (*a*) ε_{max}, (*b*) ε_{avg}.

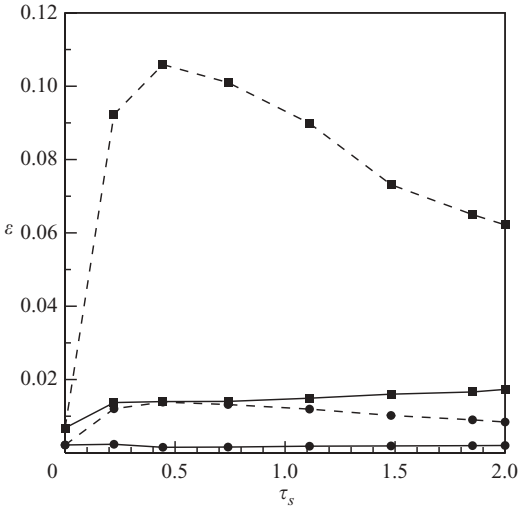

FIGURE 20. Time dependence of the fluid-speed approximation error for buffer B, $\gamma = 2$. ■, ε_{max}; ● ε_{avg} E_y was calculated from (5.4) (solid lines) and (5.6) (dashed lines). All other simulation conditions and approximations are as for figure 13.

buffer B is summarized by figure 19, which presents ε_{max} and ε_{avg} as a function of time. As for buffer A, the errors peak before $t = 0.5$ and then decay. Equation (5.4) reduces ε_{max} and ε_{avg} by as much as two-thirds from the values resulting from (5.6). By $t = 2$, $\varepsilon_{avg} < 0.003$ for all cases.

8.4. $\gamma > 1$, *Buffer B*

Sample stacking was simulated first for $\gamma = 2$ with buffer B. All other simulation conditions were as described in § 8.1. Figure 20 shows ε_{max} and ε_{avg} versus t. Since $\gamma = O(1)$ ($\alpha = O(1)$), the integral in (8.5) is important and (5.6) yields a poor approximation for E_y throughout the zone boundaries. The calculation of E_y from

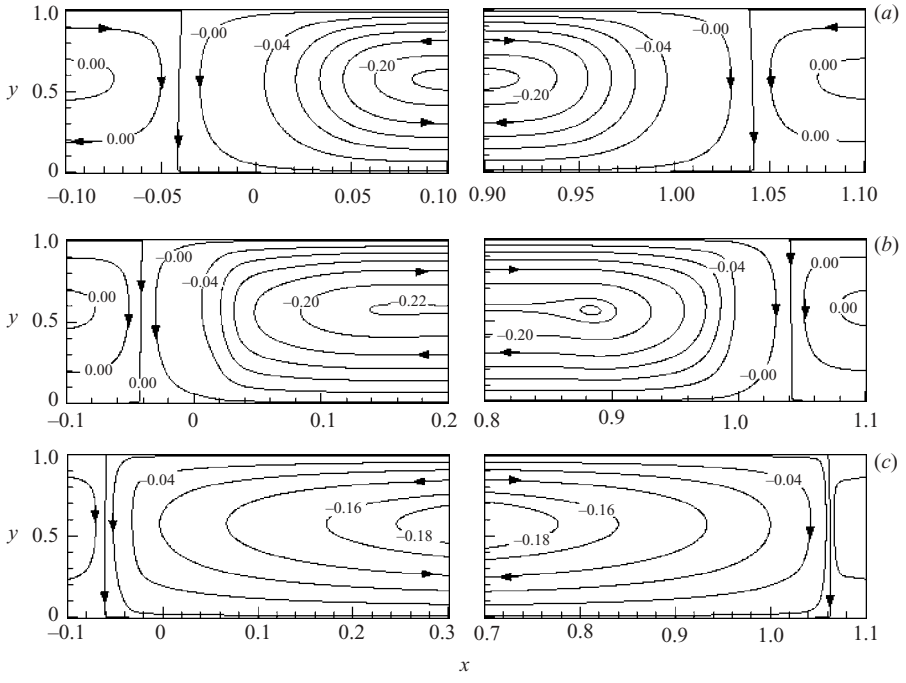

FIGURE 21. Time evolution of streamlines for buffer B, $\gamma = 5$, calculated by complete numerical solution. (*a*) $t = 0$, (*b*) $t = 0.1$, (*c*) $t = 1.0$. All other simulation conditions are as for figure 13. Unlabelled streamlines are shown for ψ from -0.16 to -0.08 at intervals of 0.04.

(5.4) rather than (5.6) reduces ε_{max} and ε_{avg} by approximately an order of magnitude, and ε_{max} never exceeds 0.03.

The maximum error peaks at a lower value than for $\gamma = 1/10$ and $\gamma = 1/50$ because E_x and u change over the length scale b throughout the zone boundary for $\gamma = 2$, since $\gamma = O(1)$; for $\gamma \ll 1$, however, the zone boundary is highly nonlinear and most of the electric-field and fluid-velocity changes occur over a narrow region near the uniform buffer.

At $\gamma = 5$, the electrical stresses begin to affect the fluid motion, but only slightly and ephemerally. As shown in figure 21, a small secondary circulation pattern develops in the downstream zone boundary, and the streamlines are slightly distorted at $t = 0.1$. As the zone boundary spreads, however, the electrical stresses quickly diminish and do not have a lasting effect. By $t = 1$, the structure of the flow begins to resemble that obtained for $\gamma < 5$. The electrical stresses do not significantly impact the fluid motion and ion transport after the initial transient, and so (5.4) and (6.11)–(6.13) still provide good approximations at $t = 2$ (figure 22).

The electrical stresses also have a significant effect on the flow for $\gamma = O(1)$ at higher values of E_0. Figure 23 shows streamlines for $\gamma = 2$ and $E_0 = 720\,\mathrm{V\,cm^{-1}}$. The electrical stresses have more influence on the flow at this condition than at $\gamma = 5$ and $E_0 = 180\,\mathrm{V\,cm^{-1}}$, and the effects last longer. Calculating these streamlines with a semi-analytic solution requires inclusion of the electrical stresses in the lubrication approximation for $\boldsymbol{u}$. Unfortunately, using (5.4) to approximate E_y in the electrical stresses in (6.7)–(6.10) results in a numerical instability in the computation. However, if $\boldsymbol{E}$ is calculated numerically the semi-analytic expressions (6.7), (6.9), and (6.10) yield good approximations for u, v, and ψ (figure 23).

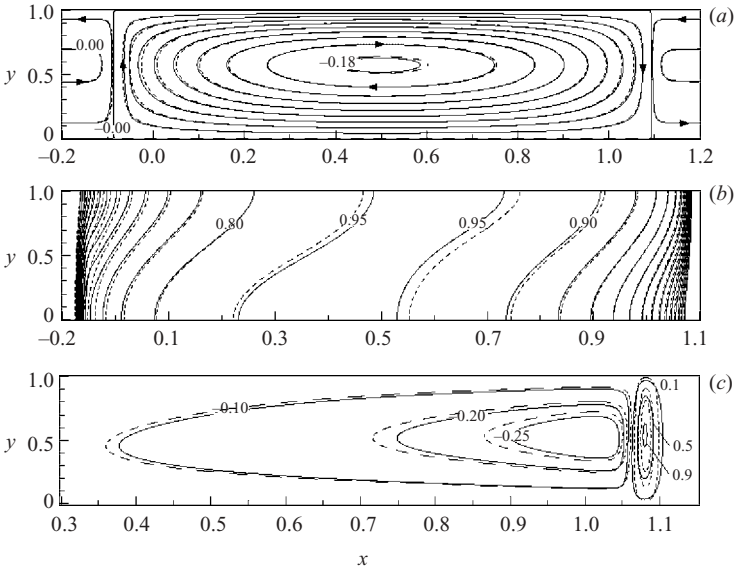

FIGURE 22. (*a*) Streamlines, (*b*) conductivity contours and (*c*) E_y contours for buffer B, $\gamma = 5$ at $t = 2$. Solid lines, complete numerical solution; dashed lines, approximate solution. E_y was calculated from (5.4); all other simulation conditions and approximations are as for figure 13. Unlabelled streamlines in top panel are shown for ψ from -0.16 to -0.02 at intervals of 0.02; conductivity contours are shown for $\sigma - 1/(1/\gamma - 1)$ from 0.25 to 0.95 at intervals of 0.05.

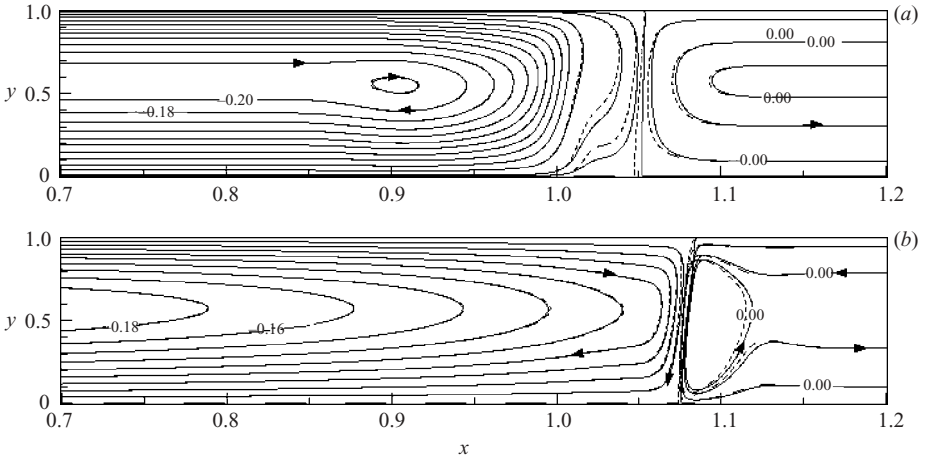

FIGURE 23. Streamlines for buffer B, $\gamma = 2$, $E_0 = 720\,\mathrm{V\,cm^{-1}}$ at (*a*) $t = 0.1$ and (*b*) $t = 1$. Solid lines, complete numerical solution; dashed lines, the approximate solution from (6.7), (6.9), and (6.10) used for $\boldsymbol{u}$ and ψ. Unlabelled streamlines are shown for ψ from -0.02 to -0.16 at intervals of 0.02. $i_0 = 5.2\,\mathrm{kA\,m^{-2}}$, $u_{eo}^0 = 4.8\,\mathrm{mm\,s^{-1}}$. All other simulation conditions are as for figure 13.

9. Concluding remarks

We have shown that for conditions typical of many microfluidic processes in non-uniform electrolytes, $\boldsymbol{u}$ and $\boldsymbol{E}$ can be calculated explicitly at any given time if the

ion distributions are known. The semi-analytic expressions for $\boldsymbol{u}$ and $\boldsymbol{E}$ increase the computation speed by a factor 4–5, and comparisons with complete numerical solutions of a prototype problem show remarkable agreement for various electrolyte conditions. Scaling arguments indicate that the approximate solutions are reasonable for a fairly liberal parameter space delineated by

$$\left(\frac{h}{b}\right)^2 \ll 1, \qquad \left(\frac{h}{b}\right)^3 Pe \ll 1, \qquad \left(\frac{h}{b}\right) Re \ll 1.$$

Numerical stability problems imply, however, that the approximation for E_y might not be sufficiently accurate to calculate the nonlinear electrical stresses when they begin to change the character of the flow, $(h/b)\lambda \geqslant O(1)$. Even with this limitation, the semi-analytic expression for $\boldsymbol{E}$ is useful for local field strengths at least up to $1\,\mathrm{kV\,cm^{-1}}$. No such restriction is imposed on the lubrication approximation for $\boldsymbol{u}$, which includes an explicit term for the electrical stresses and thus can be used for $(h/b)\lambda \geqslant O(1)$.

In microanalysis processes, solute distributions inherently evolve in time, so conductivity transition lengths b are generally not constant. The potential therefore exists for the approximations, although initially accurate, to fail during a transient sharpening of a zone boundary. Conversely, the approximations may fail initially but accurately represent the remainder of the system behaviour after spreading of the zone boundaries, as in § 8.2. Fortunately, the two-dimensional electrically driven fluid motion that creates the need to evaluate $\boldsymbol{u}$ and $\boldsymbol{E}$ in multiple dimensions also disperses the electrolyte zones. This is usually enough to maintain $\left(\frac{h}{b}\right)^2 \ll 1$, except during brief transients that have little effect on the solutions.

The analysis has also provided general information on the physical behaviour of electrokinetic processes in capillaries. Applied electric fields in rectilinear microchannels are essentially unidirectional, even when the transverse component of $\nabla\sigma$ exceeds the axial component. E_y, however, although orders of magnitude smaller than E_x, has an important effect on solutal transport when electrolyte ion mobilities are not approximately identical. Through the coupling of the ion balances to the electro-osmotic velocity, this also affects the fluid motion. E_y impacts the flow even more dramatically when $(h/b)\lambda \geqslant O(1)$, and the electrical stresses generate additional circulation patterns in conductivity-transition regions. When the electrical stresses are not significant and $(h/b)^2$, $(h/b)^3 Pe$, and $(h/b) Re \ll 1$, the axial fluid-velocity profile has a simple parabolic form.

The authors would like to acknowledge Petter E. Bjorstad at The University of Bergen Institute for Informatics, P. M. de Zeeuw at The Center for Mathematics and Computer Science (CWI), and SIAM for the freely distributed FORTRAN subroutines used to solve the PDEs for the stream function and the electric potential in the general two-dimensional numerical solution.

Note added in proof

Note that, regarding the equations following (4.13), $\langle\sigma^*\rangle$ and E_x^* are $O(1)$ unless $|\gamma_2 - \gamma_1| \ll 1$, but if $\langle\sigma\rangle$ and E_x are scaled more generally as $\langle\sigma^{**}\rangle \equiv (\langle\sigma\rangle - \sigma_0/\gamma_1)/(1/\gamma_2 - 1/\gamma_1)\sigma_0$ and $E_x^{**} \equiv (E_x - \gamma_1 E_0)/(\gamma_2 - \gamma_1)E_0$, then they are $O(1)$ for any γ_1 and γ_2. However, it is clear by inspection with the substitutions $\langle\sigma^*\rangle = \langle\sigma^{**}\rangle + \beta_1$ and $E_x^* = E_x^{**} + \beta_2$ (and similarly for C_k^* and u^*), where $\beta_{1,2} \equiv |\gamma_{1,2}/\gamma_{2,1} - 1|^{-1}$, that

this does not affect the approximations developed in the next section. The simpler scaling is used here because the inclusion of the $\beta_{1,2}$ terms simply reveals further simplification for the trivial case of $|\gamma_2 - \gamma_1| \ll 1$, but makes the equations more cumbersome and is a distraction from the general approximation development for any γ_1 and γ_2.

REFERENCES

Ajdari, A. 1996 Generation of transverse fluid currents and forces by an electric field: Electroosmosis on charge-modulated and undulated surfaces. *Phys. Rev.* E **53**, 4996–5005.

Anderson, J. L. & Idol, W. K. 1985 Electroosmosis through pores with non-uniformly charged walls. *Chem. Engng Commun.* **38**, 93–106.

Beckers, J. L. & Boček, P. 2000 Sample stacking in capillary zone electrophoresis: Principles, advantages and limitations. *Electrophoresis* **21**, 2747–2767.

Bharadwaj, R. & Santiago, J. G. 2005 Dynamics of field amplified sample stacking. *J. Fluid Mech.* **543**, 57–92.

Bier, M., Palusinski, O. A., Mosher, R. A. & Saville, D. A. 1983 Electrophoresis: Mathematical modeling and computer simulation. *Science* **219**, 1281–1287.

Bjorstad, P. 1983 Fast numerical-solution of the biharmonic Dirichlet problem on rectangles. *SIAM J. Numer. Anal.* **20**, 59–71.

Boris, J. P., Landsberg, A. M., Oran, E. S. & Gardner, J. H. 1993 LCPFCT – Flux-Corrected Transport Algorithm for Solving Generalized Continuity Equations. *NRL Mem. Rep.* 6410-93-7192. Naval Research Laboratory, Washington.

Bousse, L., Cohen, C., Nikiforov, T., Chow, A., Kopf-Sill, A. R., Dubrow, R. & Parce, J. W. 2000 Electrokinetically controlled microfluidic analysis systems. *Annu. Rev. Biophys. Biom.* **29**, 155–181.

Burgi, D. S. & Chien, R.-L. 1991 Optimization in sample stacking for high-performance capillary electrophoresis. *Anal. Chem.* **63**, 2043–2047.

Gebauer, P. & Bocek, P. 2002 Recent progress in capillary isotachophoresis. *Electrophoresis* **23**, 3858–3864.

Ghosal, S. 2002 Lubrication theory for electro-osmotic flow in a microfluidic channel of slowly varying cross-section and wall charge. *J. Fluid Mech.* **459**, 103–128.

Ghosal, S. 2003 The effect of wall interactions in capillary-zone electrophoresis. *J. Fluid Mech.* **491**, 285–300.

Ghosal, S. 2004 Fluid mechanics of electro-osmotic flow and its effect on band broadening in capillary electrophoresis. *Electrophoresis* **25**, 214–228.

Gottlieb, D. 1972 Strang-type difference schemes for multidimensional problems. *SIAM J. Numer. Anal.* **9**, 650–661.

von Helmholtz, H. 1879 Stüdien Über electrische grenschichten. *Ann. Phys.* **7**, 337–387.

Ikuta, N. & Hirokawa, T. 1998 Numerical simulation for capillary electrophoresis I. Development of a simulation program with high numerical stability. *J. Chromatogr.* A **802**, 49–57.

Kasicka, V. 1997 Theoretical bases and separation principles of capillary electromigration methods. *Chemicke Listy* **91**, 320–329.

Leal, L. G. 1992 *Laminar Flow and Convective Transport Processes.* Butterworth-Heinemann.

Long, D., Stone, H. A. & Ajdari, A. 1999 Electro-Osmotic flows created by surface defects in capillary electrophoresis. *J. Colloid Interface Sci.* **212**, 338–349.

Martens, J. H. P. A., Reijenga, J. C., ten Thije Boonkkamp, J. H. M., Mattheij, R. M. M. & Everaerts, F. M. 1997 Transient modelling of capillary electrophoresis isotachophoresis. *J. Chromatogr.* A **772**, 49–62.

Mitchell, P. 2001 Microfluidics—downsizing large-scale biology. *Nature Biotechnol.* **19**, 717–721.

Mosher, R. A., Saville, D. A. & Thormann, W. 1992 *The Dynamics of Electrophoresis.* VCH, Weinheim.

Palusinski, O. A., Graham, A., Mosher, R. A., Bier, M. & Saville, D. A. 1986 Theory of electrophoretic separations. Part II: Construction of a numerical scheme and its applications. *AIChE J.* **32**, 215–223.

Russel, W. B., Saville, D. A. & Schowalter, W. R. 1989 *Colloidal Dispersions*. Cambridge University Press.

Saville, D. A. & Palusinski, O. A. 1986 Theory of electrophoretic separations. Part I: Formulation of a mathematical model. *AIChE J.* **32**, 207–214.

von Smoluchowski, M. 1903 Contribution à la théorie de l'endosmose électrique et de quelques phenomènes corrélatifs. *Bull. Intl Acadé. Sci. Cracovie* **8**, 182–200.

Sounart, T. L. 2001 Electrokinetic transport and fluid motion in microanalytical electrolyte systems. PhD Dissertation, The University of Arizona.

Sounart, T. L. & Baygents, J. C. 2000 Simulation of electrophoretic separations by the flux-corrected transport method. *J. Chromatogr.* A **890**, 321–336.

Sounart, T. L. & Baygents, J. C. 2001 Electrically-driven fluid motion in channels with streamwise gradients in the electrical conductivity. *Colloids Surfaces* A*: Physicochem. Engng Aspects* **195**, 59–75.

Stone, H. A., Stroock, A. D. & Ajdari, A. 2004 Engineering flows in small devices: Microfluidics toward a lab-on-a-chip. *Annu. Rev. Fluid Mech.* **36**, 381–411.

Sweby, P. K. 1984 High resolution schemes using flux limiters for hyperbolic conservation laws. *SIAM J. Numer. Anal.* **21**, 995–1011.

Taylor, G. I. 1953 Dispersion of soluble matter in solvent flowing slowly through a tube. *Proc. R. Soc. Lond.* A **219**, 186–203.

Thormann, W., Zhang, C.-X., Caslavska, J., Gebauer, P. & Mosher, R. A. 1998 Modeling of the impact of ionic strength on the electro-osmotic flow in capillary electrophoresis with uniform and discontinuous buffer systems. *Anal. Chem* **70**, 549–562.

de Zeeuw, P. M. 1990 Matrix-dependent prolongations and restrictions in a blackbox multigrid solver. *J. Comput. Appl. Math.* **33**, 1–27.